Nuclear Inst. and Methods in Physics Research, A 896 (2018) 1–23

Contents lists available at ScienceDirect

Nuclear Inst. and Methods in Physics Research, A

journal homepage: www.elsevier.com/locate/nima

The network of photodetectors and diode lasers of the CMS Link alignment system

P. Arce [a], J.M. Barcala [a], E. Calvo [a], A. Ferrando [a,*], M.I. Josa [a], A. Molinero [a], J. Navarrete [a], J.C. Oller [a], J. Brochero [b], A. Calderón [b], M.G. Fernández [b], G. Gómez [b], F.J. González-Sánchez [b], C. Martínez-Rivero [b], F. Matorras [b], T. Rodrigo [b], P. Ruiz-Árbol [b], L. Scodellaro [b], M. Sobrón [b], I. Vila [b], A.L. Virto [b], J. Fernández [c], P. Raics [d], Zs. Szabó [d], Z. Trócsnyi [d], B. Ujvári [d], Gy. Zilizi [d], N. Béni [e], G. Christian [e], J. Imrek [e], J. Molnar [e], D. Novak [e], J. Pálinkás [e], G. Székely [e], Z. Szillási [e], G.L. Bencze [f], G. Vestergombi [f], M. Benettoni [g], F. Gasparini [g], F. Montecassiano [g], M. Rampazzo [g], M. Zago [g], A. Benvenuti [h], H. Reithler [i], C. Jiang [j]

[a] CIEMAT, Madrid, Spain
[b] Instituto de Física de Cantabria, CSIC-University of Cantabria, Santander, Spain
[c] University of Oviedo, Oviedo, Spain
[d] University of Debrecen, Institute of Experimental Physics, Debrecen, Hungary
[e] Institute of Nuclear Research ATOMKI, Debrecen, Hungary
[f] KFKI Research Institute for Particle and Nuclear Physics, Budapest, Hungary
[g] Dipartimento di Fisica dell'Universita di Padova e Sezione dell'INFN, Padova, Italy
[h] Dipartimento di Fisica dell'Universita di Bologna e Sezione dell'INFN, Bologna, Italy
[i] Physikalisches Institut IIIA, RWTH Aachen University, Aachen, Germany
[j] Institute of High Energy Physics, Beijing, China

ARTICLE INFO

Keywords:
CMS
Alignment
Amorphous silicon photodetectors

ABSTRACT

The central feature of the CMS Link alignment system is a network of Amorphous Silicon Position Detectors distributed throughout the muon spectrometer that are connected by multiple laser lines. The data collected during the years from 2008 to 2015 is presented confirming an outstanding performance of the photo sensors during more than seven years of operation. Details of the photo sensor readout of the laser signals are presented. The mechanical motions of the CMS detector are monitored using these photosensors and good agreement with distance sensors is obtained.

1. Introduction

A major part of the Compact Muon Solenoid detector (CMS) [1–4] is a powerful muon spectrometer [3] that identifies and measures muons over a wide range of energy from a few GeV up to several TeV. The CMS detector basically has a cylindrical symmetry around the LHC beam pipe, an overall diameter of 15 m, a total length of 21.6 m and weighs 12.5 kt (mainly iron flux return). At its heart, a 13 m long, 6 m inner diameter superconducting solenoid [2] provides a 3.8 T field along the beam axis and a bending power of about 12 Tm in the transverse plane. The field return consists of 1.5 m of iron layers interspersed with four muon stations in both the barrel and endcap regions that ensure full geometrical coverage and sufficient redundancy.

The accuracy required in the position measurement of the muon chambers is driven by the resolution desired in the momentum measurement of high energy muons. CMS is designed to achieve a combined (Muon System [3] and Tracker [4]) momentum resolution of 0.5%–1% for $p_T \approx 10$ GeV, 1.5%–5% for $p_T \approx 100$ GeV and 5%–20% for $p_T \approx 1$ TeV for the region $|\eta| < 2.4$. This momentum resolution requires the knowledge of the position of the chambers with a precision comparable to their resolution.

Simulation studies were performed [5] to quantify the importance of muon chamber location for the momentum resolution. The solenoidal magnetic field bends charged particles in $r\phi$, the most important coordinate for determining the muon momentum. Hence, the alignment system should reconstruct the position of the chambers within 150–300

* Corresponding author.
E-mail address: antonio.ferrando@ciemat.es (A. Ferrando).

https://doi.org/10.1016/j.nima.2018.04.004
Received 10 January 2018; Received in revised form 12 March 2018; Accepted 4 April 2018
Available online 16 April 2018

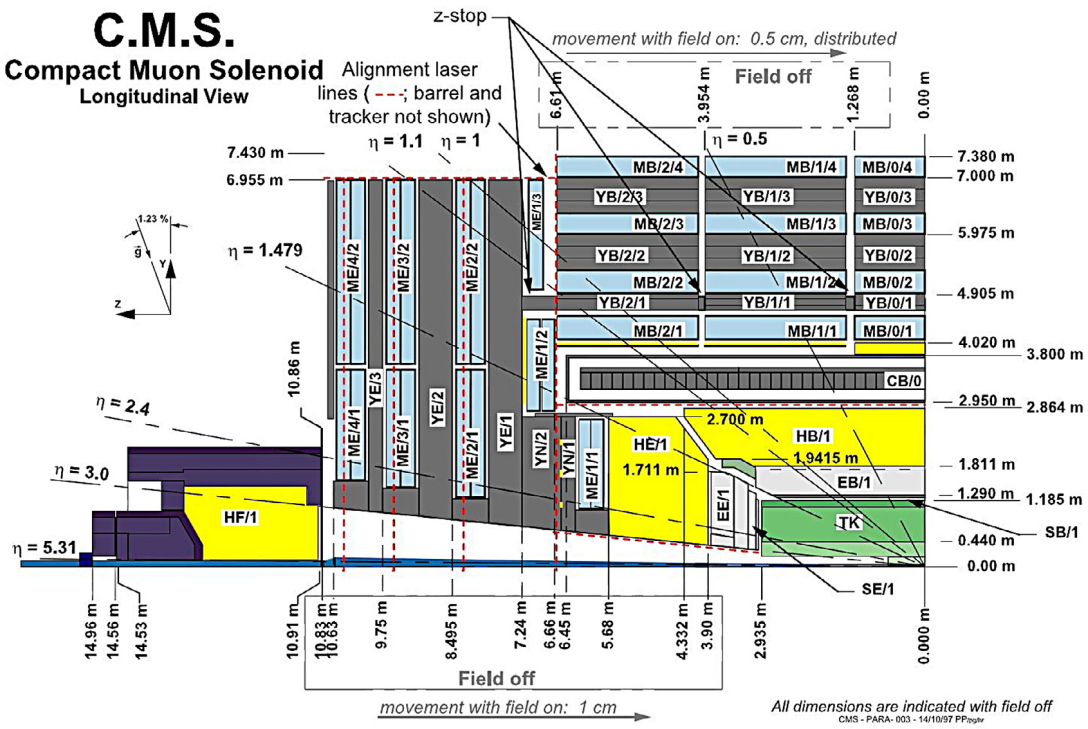

Fig. 1. Longitudinal view of one quadrant of the CMS detector. Laser lines (in dashed) used for the Alignment System are shown, except for the barrel region. The position of the Z-stops is also indicated. The floor of the detector has a small inclination of about 1.23% with respect to the gravity vector **g** as depicted in the small drawing on the left.

μm for MB1–MB4 and within 75–200 μm for ME1–ME4 (Fig. 1). The tighter constraints correspond to the first stations (MB1 and ME1) since the magnetic bending in the return yoke is reversed with respect to the magnetic field in the solenoid and hence the largest bending and best momentum determination is measured in the first stations. Since these stations are located immediately outside the magnet before the flux return they combine with the Tracker hits to achieve the measurement of the muon momentum.

During CMS operations, the movements and deformations of the muon spectrometer are surely larger than 100 μm. To monitor these motions, CMS is instrumented with an opto-mechanical alignment system that performs a continuous and precise measurement of the relative positions of the muon chambers as well as the position of the muon spectrometer with respect to the tracker, which is aligned independently.

In a previous document [6] the alignment system was presented, and, data taken during the two phases of the 2006 Magnet Test and Cosmic Challenge measured the effects of the ramp up and down in the magnetic field (magnetic cycle). It was shown that the Link system produces geometrical reconstructions of relative spatial locations and angular orientations between the muon chambers and the tracker body with a resolution better than 150 μm for distances and about 40 μrad for angles.

The structural equilibrium of the muon spectrometer was also investigated [7,8]. Using alignment data from the years 2008 and 2009, it was found that once the magnetic field intensity reaches 3.8 T, provided that the current in the coils remains unaltered, the mechanical structures reach equilibrium within the first 24 h. Structural equilibrium means that any displacement in any direction (axial or radial) remains within the short distance sensors resolution: ±40 μm and any rotation within the tilt sensors resolution: ±40 μrad. These structural equilibrium periods will be referred to as stability periods.

To achieve a precise multipoint position monitoring, one needs to measure and/or monitor accurately the space position of a laser beam at several points along its path. In such cases the simplest solution is to use transparent position sensors attached to the pieces whose spatial positions have to be monitored. When the expected independent motions of the pieces are big (i.e. from mm to a couple of cm) the active area of the sensors must be large.

This paper focuses on the description of the CMS Link alignment network of diode lasers and photosensors and presents a brief analysis of the corresponding recorded data during the physics runs in the periods 2008 to 2013 and in 2015. The goal is to show how the photosensors behave during the magnet cycles and the stability periods, how compatible these measurements are with previous studies [7] and how their data are used to help in the CMS geometrical reconstruction.

A short description of the CMS Alignment system is given in Section 2. The general layout, the electronic equivalence and the measurement principle of the amorphous silicon position detectors (ASPDs), as well as the readout electronics are shown in Sections 3, 4 and 5, respectively. A summary of the characteristics of the sensors, their average performance and the tests prior to their installation in CMS are described in Section 6, while Section 7 deals with the description of the network of photo sensors and diode lasers of the CMS Link alignment system. The interpretation of the motions detected by the light spot reconstruction is given in Section 8 and an analysis of those reconstructions during the magnet cycles and the stability periods is done in Section 9. Section 10 shows, with a few examples, how the CMS motions detected with the ASPDs, during the ramping of the magnetic field, correlate with those obtained from the distance-measuring potentiometers (short distance sensors) used in previous studies [6–8]. Finally, Section 11 summarizes the results.

2. The CMS alignment system

The CMS tracking detectors are grouped into four separate systems: two endcaps, the central barrel, and the tracker, which is inside the solenoidal coil. Different muon detection technologies are employed for the central and the endcap regions due to the different backgrounds and the varying intensity and homogeneity of the magnetic field. A

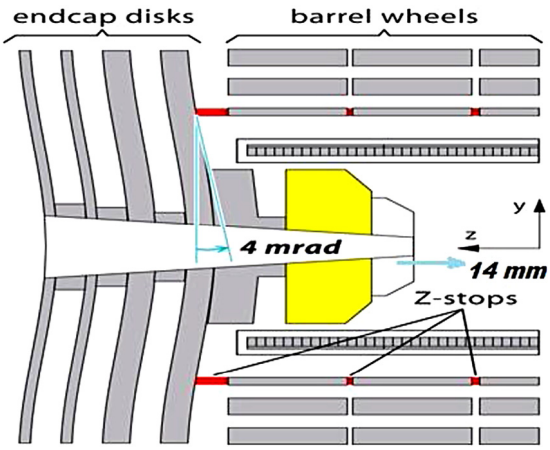

Fig. 2. Sketch of the deformation of the endcap iron disks as a result of the compression due to the magnetic field forces and the resistance of the barrel Z-stops.

longitudinal view of one quadrant of the CMS experiment showing the various detectors is given in Fig. 1.

In the barrel region, surrounding the coil of the solenoid, four concentric stations of drift tube (DT) chambers (named MB1 to MB4), are inserted in the five wheels that constitute the return iron yoke. A muon chamber is composed of three superlayers. Each superlayer in turn is made of four layers of drift cells, the basic detection unit. Drift times are translated into local space positions with a single hit resolution of 250 μm. Superlayers are arranged to measure the muon in two orthogonal coordinates; two superlayers measure the muon in the bending plane, and the third superlayer measures it in the beam axis direction.

The mechanical design of a drift chamber is driven by the 100 μm spatial precision requirement in the determination of the track position in the bending plane. Track segments are obtained by linear fits to the reconstructed hits in each coordinate. The DT chambers are subject to variable residual magnetic fields below 0.4 T for all the stations except for the innermost MB1 chambers closest to the endcaps, where the field reaches 0.8 T.

At both CMS endcaps there are four layers of muon chambers, named ME1 to ME4. In the endcap regions the magnetic field is typically high and very inhomogeneous due to its bending of the flux return. In addition, at the level of the ME1 chambers the field intensity may be as high as 3 T. To cope with this and with the high particle fluxes in these regions, different gas ionization detectors called Cathode Strip Chambers (CSCs) are used. The CSCs are multi-wire proportional chambers in which the cathode plane is segmented into strips running across wires, giving 2D information of the particle passage. The flux return results in a reversal of the magnetic force on a muon so the best measure of the muon momentum occurs in the first station, which has the highest resolution requirement (75 μm). The remaining muon stations require a lower precision of 150 μm.

Resistive Plate Chambers (RPCs), both in the barrel and in the endcaps, complement the muon spectrometer. They are used mainly for trigger purposes since their time resolution is better than 2 ns, although their hits may also participate in the muon track recognition. The RPCs are assumed to be placed at their nominal positions within their spatial resolution of about 1 cm.

Typically, the total number of hits including tracker hits registered along a muon track is about 40–45 in the forward region and about 55 in the central one ($|\eta| < 1$). The muon momentum is measured through the bending of its track in the transverse plane. The radius of curvature ρ and the momentum of the muon in the plane perpendicular to the magnetic field (p_T) are related by $\rho[\mathrm{m}] = p_T\ [\mathrm{GeV}]/0.3\ \mathrm{B[T]}$. The radius of curvature is obtained from the measurement of the muon trajectory sagitta s, after traversing a distance d in the magnetic field, using the approximate expression $\rho = d^2/8$ s. An uncertainty in the sagitta measurement results in an uncertainty in the momentum measurement.

The relative uncertainty in the sagitta measurement is $\delta s/s = -\delta p_T/p_T$, proportional to $\sigma(s)p_T/d^2B$, where $\sigma(s)$ is the resolution in the sagitta measurement. The relative uncertainty in the momentum increases with the muon momentum and decreases linearly with the magnetic field and quadratically with the traversed distance.

A right-handed coordinate system is used in CMS, with the origin at the nominal interaction point (IP), the x-axis pointing to the centre of the LHC ring, the y-axis pointing up (perpendicular to the LHC plane), and the z-axis along the anticlockwise beam direction. The polar angle θ is measured from the positive z-axis and the azimuthal angle ϕ is measured in the xy-plane. The pseudorapidity is a geometrical variable defined as $\eta = -\ln[\tan(\theta/2)]$.

At 3.8 T the solenoid induces an axial force of about 10,000 tons on the endcap iron yokes in the direction of the IP. Aluminium blocks, called Z-stops, are located between the endcap disks and the barrel region, as well as between the five barrel wheels, to prevent the different structures from being crushed into each other. The positions of the Z-stops are indicated in Fig. 1. The deformation of the endcap iron disks as a result of the compression due to the magnetic forces and the resistance of the barrel Z-stops are illustrated in Fig. 2.

To meet the momentum resolution requirements the tracker is equipped with an internal alignment system and can be treated as a rigid body for purpose of the muon alignment system. The CMS Alignment System is therefore organized in three basic blocks:

– The Tracker alignment system [4] measures the relative position of the various tracker modules and monitors eventual internal deformations.

– The Muon (Barrel and Endcaps) alignment system [3] monitors the relative positions among the DT and CSC muon chambers.

– The Link alignment system [3] connects the position of the two muon subsystems, Barrel and Endcaps, to the position of the Tracker and monitors the relative movements between them.

The positions of the Link system sensors define three alignment planes 60° apart, starting at $\Phi = 15°$. Fig. 3(left) shows one of the Φ planes where the three alignment subsystems can be seen. Each plane contains four independent alignment quadrants where the three systems are connected.

In each Φ quadrant six Amorphous Silicon Position Detector sensors (ASPDs) are connected by laser lines. The full network contains 36 sensors per CMS endcap. An ASPD sensor [8–10] consists of two groups of 64 silicon micro-strips 408 μm wide, with a pitch of 430 μm, oriented perpendicularly. The total active area is $\sim 30 \times 30\ \mathrm{mm}^2$.

The measured spatial resolutions of the reconstructed light spot on the sensor active area are, on average, 5.2 ± 2.6 μm and 5.1 ± 2.4 μm for the X- and Y-sensor coordinates, respectively [10].

Each of the 12 alignment quadrants use four laser light paths, one originating at the Tracker, two at the Endcap, and one at the Barrel region as indicated in Fig. 3(left), resulting in 48 laser paths, 24 on each side (positive or negative Z) of the detector. Each laser path, in turn, is monitored by three ASPDs, providing a total of 144 beam spots over the whole CMS detector.

All laser-source collimators are housed in rigid carbon fibre structures called alignment rings (AR), modules for the alignment of the barrel (MAB), and link disks (LD) as shown in Fig. 3(left).

The ARs are annular structures attached to the Back Disks (BDs), the outermost, uninstrumented, Tracker Endcap disks. The LDs, annular structures as well, are suspended from the inner diameter of the YN1 iron disks of the endcap muon spectrometer by means of aluminium tubes attached to mechanical assemblies called Transfer Plates (TPs). MABs are mounted onto the barrel yoke elements.

The assumption of “rigid bodies” for the four tracking systems, allows setting up a redundant system of twelve planes that provide

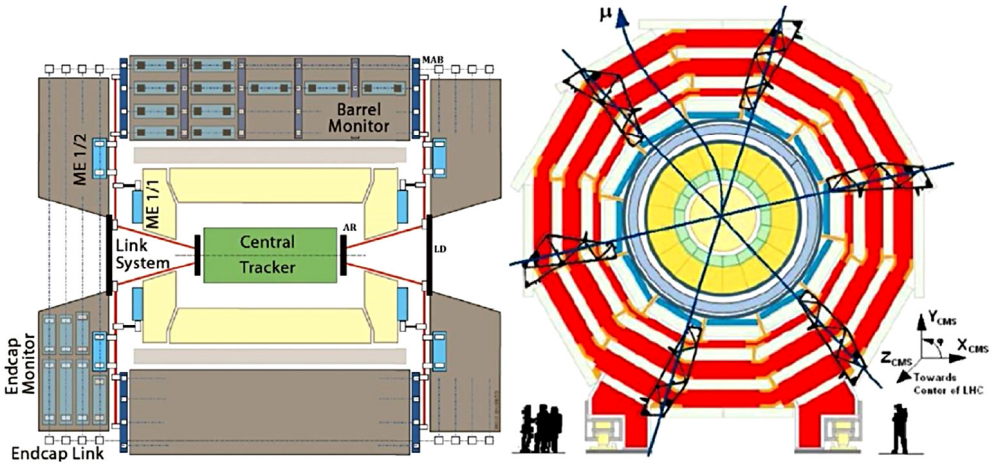

Fig. 3. Schematic view of the Alignment System. (Left): one Φ alignment plane. The continuous and dotted lines show different optical paths. (Right): transverse view of the barrel muon detectors. The crossing lines indicate the three alignment Φ planes with sketches of the six Modules for the Alignment of the Barrel (MABs). The CMS coordinate system is also indicated in the figure.

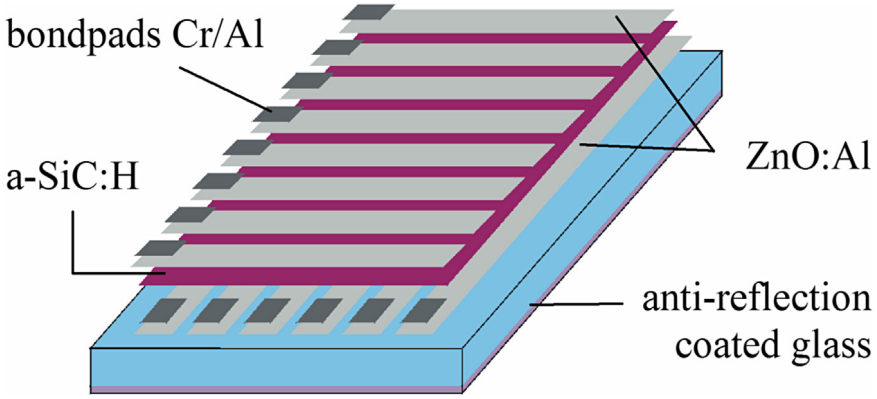

Fig. 4. Sketch of the ASPD sensor structure. The 64 × 64 sensor array covers an area of 30 × 30 mm^2 including the bond pads. Fine-tuning and precise control of the optical properties and film thicknesses of the top and bottom ZnO:Al strips and of the non-patterned a-SiC:H photoconductor enable a maximum optical transmittance T ≈ 85% at the design wavelength λ_L(681 nm).

redundancy in case of a malfunctioning sensor or a missing signal due to large mechanical movements [8]. The Φ Link planes are also depicted in Fig. 3(right), where the CMS coordinate system is also indicated.

The Link System laser-ASPD network is complemented by electrolytic tiltmeters for angular measurements with respect to the gravity, optical and mechanical proximity sensors for short distance measurements, aluminium tubes for long distance measurements, magnetic probes and temperature sensors [6–8]. All sensors are located inside independent rigid structures, which are individually calibrated and intercalibrated on special benches and measured later, by photogrammetry [6], after installed in CMS.

3. Amorphous silicon position detecting sensors

The use of semi-transparent photodetectors is very appropriate for the CMS Link Alignment System due to the fact that optical paths should cross more than one sensor in the same laser line, as can be inferred from Fig. 3(left).

This is not the unique solution to achieve that purpose, but it is probably the simplest one and this is why groups at IFCA and CIEMAT, together with Steinbeis-Transferzentrum für Angewandte Photovoltaik und Dünnschichttechnik (STAPD), carried out a joint effort to develop a new generation of semi-transparent amorphous silicon 2D photosensors (ASPD) for multipoint position detecting purposes. The set of ASPD sensors for CMS was manufactured by STAPD with technological support from the Universität Stuttgart (Institut für Physikalische Elektronik, IPE) under the quality control and acceptance of IFCA–CIEMAT. A complete report on this work can be found in Ref. [11].

Fig. 4 depicts the layer sequence and the general layout of these semi-transparent 2D sensors. A matrix arrangement of perpendicular ZnO strips enables the precise reconstruction of the position of the laser beam, while the a-SiC:H layer sandwiched between the ZnO strips provides high optical transmission and photosensitivity at the same time. The union of a ZnO strip and the photoconducting a-SiC:H defines a Schottky photodiode strip. The position of a light spot onto the sensor surface is then reconstructed as the centroid of the local photo responses generated by the 2D matrix of photodiode strips.

The ASPD sensors incorporate antireflective coated glass substrates delivered by Schott Advanced Materials (Grünenplan, Germany). These are special 100 mm diameter glass wafers with a high stability against irradiation damage that are selected from a production lot for minimum deviation in parallelism of their two surfaces. The maximum deviation in thickness was 5 μm. Those high-quality glass wafers receive a very homogeneous antireflective coating by Jenoptik (Jena, Germany) which reduces reflection losses to less than 0.5% per surface.

By optimizing material properties, deposition, and patterning processes, we achieve a layer sequence, which represents an optimum compromise between optical transparency and photosensitivity. This optimized ASPD sensor comprises the following layer sequence: antireflective coated glass substrate (1 mm), aluminium doped zinc oxide

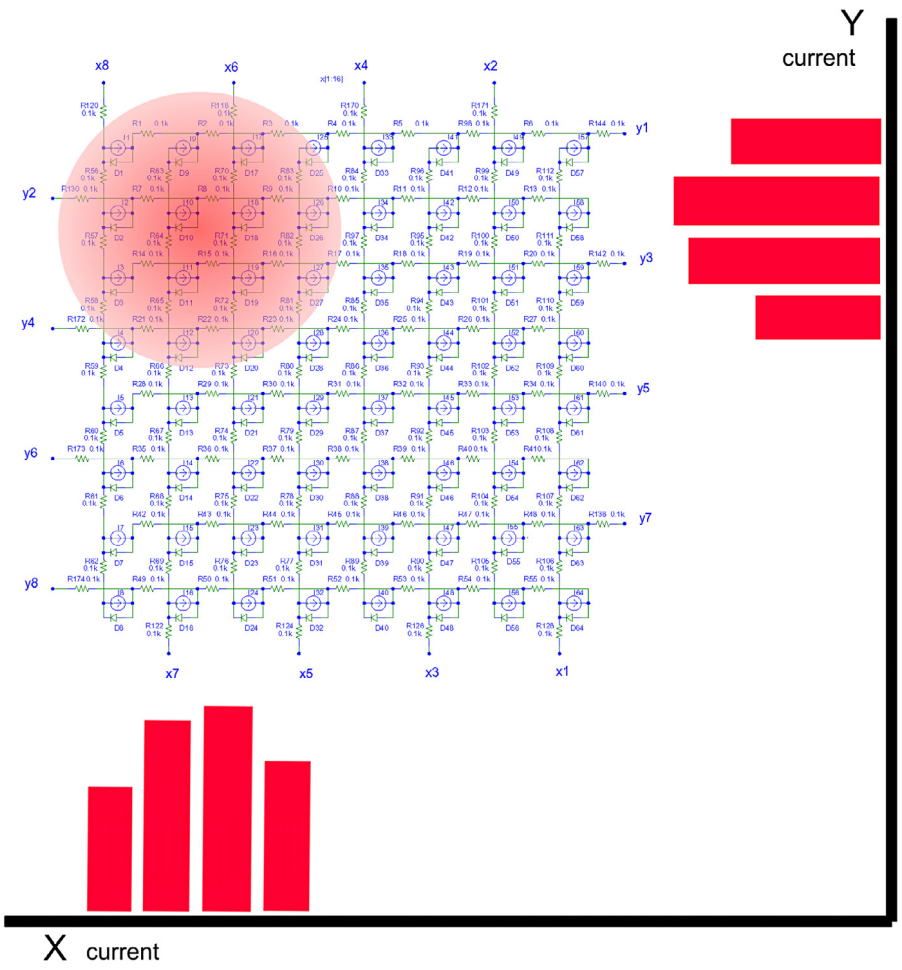

Fig. 5. Example of the electronic equivalence of an 8 X 8 strips ASPD sensor, with a sketch of the readout current distributions generated by a light spot illuminating 4 strips in each direction.

ZnO:Al (110 nm), carbon-doped hydrogenated amorphous silicon a-$Si_{0,9}C_{0,1}$:H (195 nm), and ZnO:Al (110 nm).

Top and bottom strips are arranged perpendicular to each other. The width of each ZnO:Al strip amounts to 408 μm, with a 22 μm spacing to the neighbouring strips. Aluminium bond pads arranged on top of the ZnO:Al strips outside the photosensitive area of the sensors provide electric contact to the individual strips by wire bonding to the readout electronics board, described later.

4. ASPD readout

The photodiodes of the ASPDs are read out in the following way: if $N_{x(y)}$ is the number of photodiodes along the two orthogonal coordinates $x(y)$, they are accessed as a set of $N_x + N_y$ rows and columns of photocurrents.

Fig. 5 illustrates the electronic equivalent circuit for the case of a small 8×8 strips sensor with a light spot illuminating 4 strips in each direction. The photocurrents generated in each strip diode are extracted through the "x_i" and "y_i" ends. Measuring the photocurrents going through "y_1", "y_2"…., "y_8" and "x_1", "x_2"…, "x_8" terminals, the projections over the Y and X axis of the light spot intensity are obtained, which are also indicated in the figure.

In practice, the two coordinates of the light spot centre on the sensor sensitive area are determined by double Gaussian fits to the Y and X light distributions, respectively. A double Gaussian function is used to account for a possible small amplitude, but large width contribution caused by background.

Fig. 6(top) and (bottom) show the reconstruction of X and Y coordinates of a laser beam spot incident on the sensor. The curves are the result of fits to the corresponding photocurrent distributions. The distributions in the insets show the charge collected from each of the strips (in ADC counts).

In this particular example the effective widths of the double Gaussians, calculated as the amplitude-weighted quadrature sum of the widths of each of them, are 542.0 μm and 537.0 μm in the X and Y coordinates, respectively. The uncertainty in the reconstructed light spot coordinates in the example is 36.1 μm and 35.8 μm for the X and Y coordinates, respectively. The uncertainties in the X and Y positions are calculated as the effective width of the double Gaussian fit divided by the square root of the number of strips used in the reconstruction (typically 15 if there are no bad strips),

The goodness of the Gaussian fits is not uniform over the full sensitive area. Although the response in terms of mA/W is very homogeneous, the presence of any "bad strips" in the beam spot area diminishes the degrees of freedom in the Gaussians fits to the current distributions. A strip is called "bad" if it does not provide any electrical signal useable for the light spot centre reconstruction.

Electrical defects that may occur during ASPD processing can be classified into two main types. First, an in-plane connection between two neighbouring strips causes the photocurrent signals of both neighbouring strips to approximately double under uniform illumination. The second major type of defect is a short circuit through the layer stack in the vertical direction. Particles from the environment or from a deposition tool are electrostatically captured at the glass substrate. Such adsorbed particles may be released at any stage of the processing

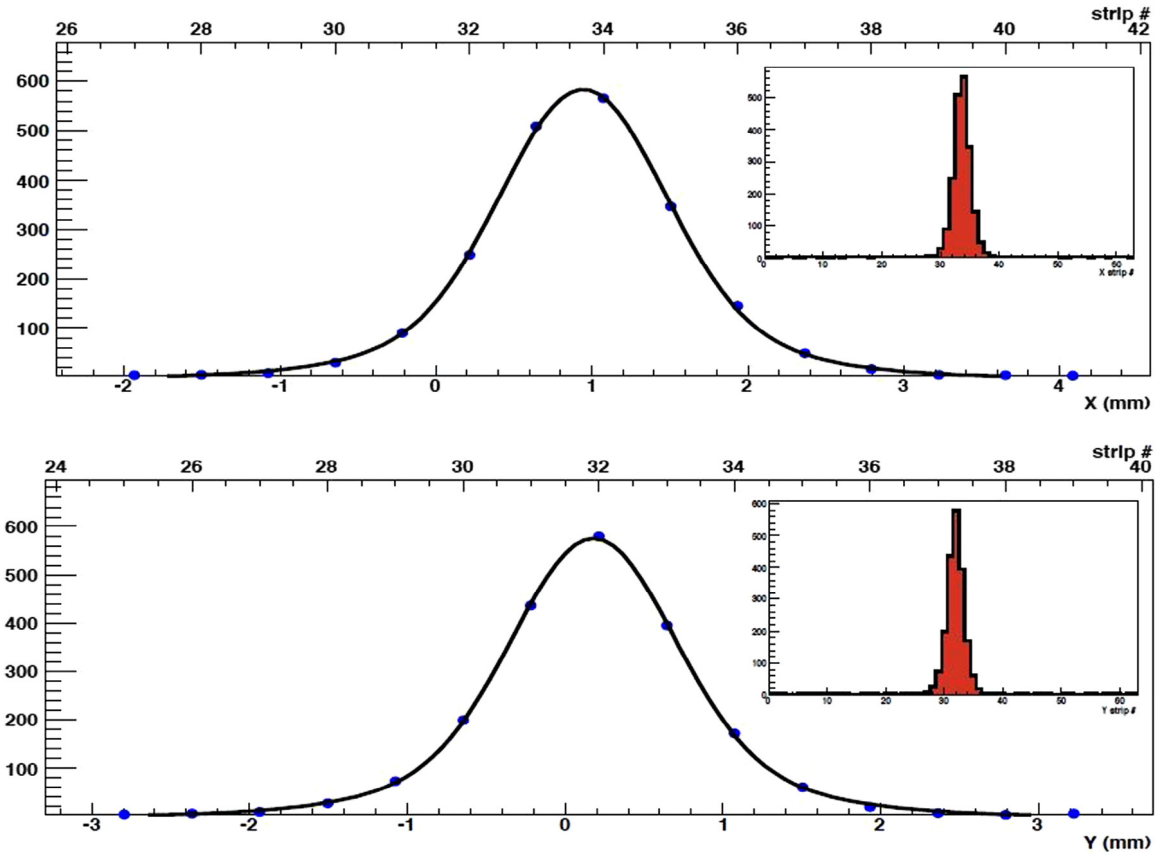

Fig. 6. Example of the spot signal reconstruction on the local to the sensor X (top) and Y (bottom) coordinates from the currents readout of the vertical and horizontal strips, respectively. The inset drawings show the actual readout currents from the illuminated vertical (up) and horizontal (down) strips.

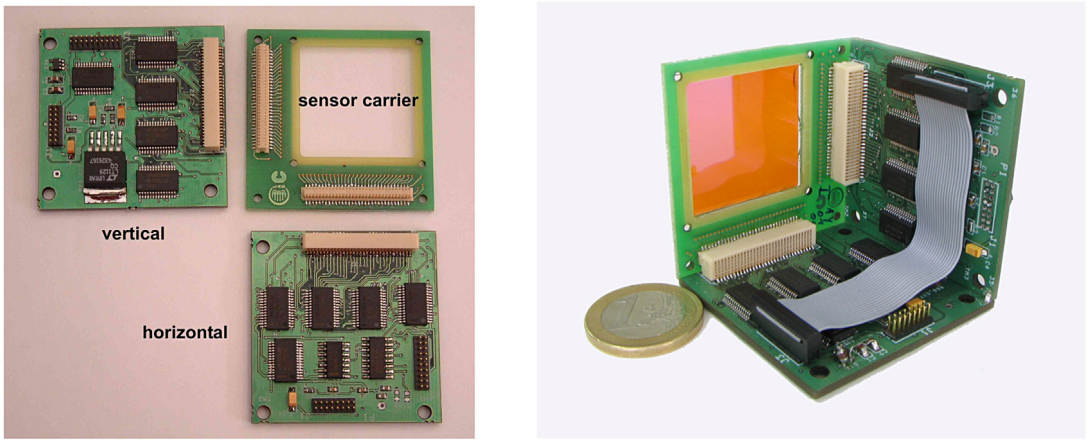

Fig. 7. The photograph on the left shows the sensor carrier board with place for sensor accommodation and two perpendicular lines of 64 aluminium terminated pads for sensor electronics bonding. Also visible are the "horizontal" and "vertical" boards of the ASPD FE electronics, with their various components: resistors, capacitors, the 16:1 multiplexers and the "male" miniature connectors to extract the signals. The photograph on the right shows the final compact form, whose dimensions are: $4.7 \times 4.7 \times 4.7$ cm^3.

sequence forming a pinhole. Depending on the specific processing step, the resulting defect introduces a vertical electric contact between the top and bottom ZnO:Al strips. As a consequence, the affected row(s) and column(s) of the sensor will exhibit an electrical response independent of the illumination.

5. Readout electronics

Custom electronics for the readout of the sensor photocurrents and the subsequent Gaussian fits has been designed and constructed at CIEMAT. The electronics consists of a sensor carrier, holding the sensor, coupled to the front-end (FE) electronics (two signal multiplexer boards) and a signal processor or Local Electronic Board (LEB).

5.1. The sensor carrier and the signal multiplexer boards

The ASPD sensor is mounted on the carrier board with two perpendicular pads containing 64 gold-terminated pads for reading out the signals of the sensor. Two 64-pin miniature connectors link the photocurrents from the ASPD sensor to the multiplexer boards.

(a)

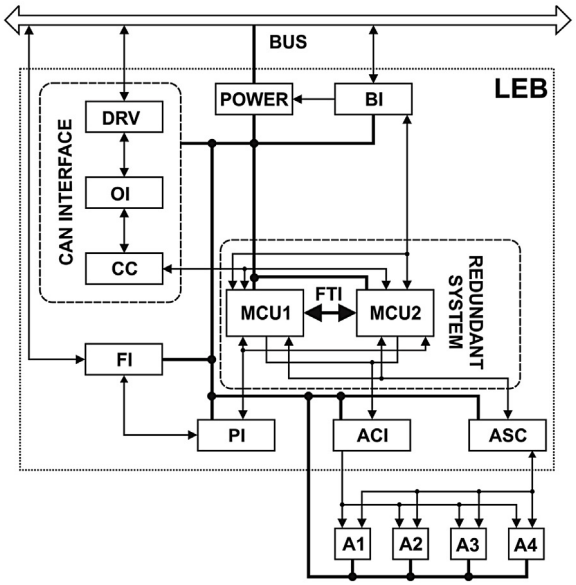

(b)

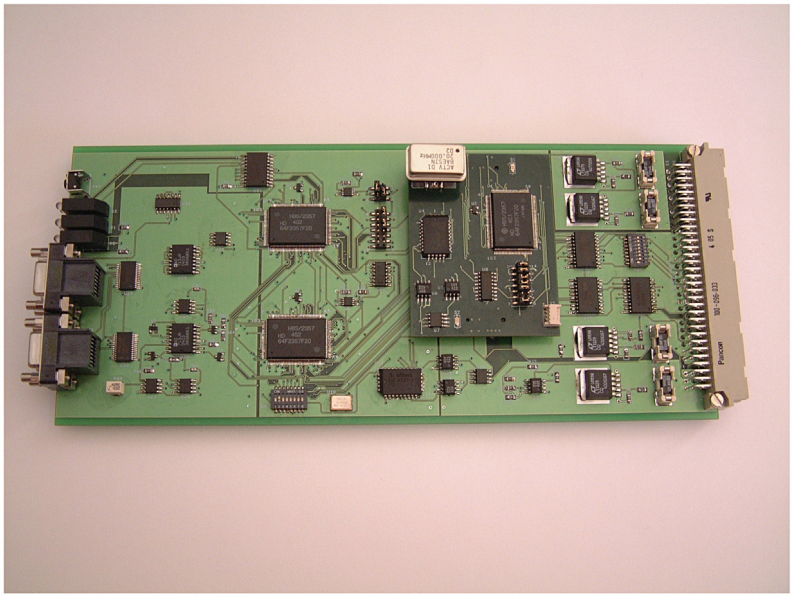

Fig. 8. (a) Diagram of the LEB readout card showing the various integrated blocks: Bus Interface (BI), CAN bus Interface (CI), ASPD Control Interface (ACI), ASPD Signal Conditioner (ASC), Micro Controller Units (MCU), Fault Injection board Interface (FI) and the Programming Interface (PI). (b) Photograph of a Local Electronic Board (LEB) where the blocks described in the text and in the diagram in (a) are installed.

The multiplexer boards (named "horizontal" and "vertical") are each mounted perpendicular to the carrier board as shown in Fig. 7(left). These multiplexer boards accept currents from the ASPD sensor as well as control signals from the LEB.

Eight multiplexers (16:1), for photocurrent switching, are mounted on the boards. Four multiplexers (64 channels) are used for the top electrodes (y-axis vertical multiplexers) and the other four (64 channels) for the bottom electrodes (x-axis horizontal multiplexers).

To bias the Schottky photodiodes, which are the active elements of the ASPD, each top electrode of the sensor is connected to analog ground (AGND) through a 47 kΩ resistor and each bottom electrode, in turn, is connected to the analog bias voltage (ABIAS) through a similar 47 kΩ resistor. Each strip of the bottom and top electrodes is connected to a multiplexer input.

The sensor carrier and the multiplexer boards are mounted in an open-cube set-up, with only three faces as shown in Fig. 7(right), of 4.7 cm per side. This arrangement is a technical solution that minimizes the dimensions of the complete detector unit to 4.7×4.7 cm^2 in the plane perpendicular to the light path.

5.2. Local Electronic Board (LEB)

The Local Electronic Board is the signal processor board that controls the ASPD readout. It converts current to voltage, digitizes analog signals, reconstructs the light beam spatial position coordinates and communicates with a central PC. A single LEB can control up to 4 ASPD sensors simultaneously.

The LEB board block diagram is shown in Fig. 8(a). In the Link alignment system, the LEBs communicate with each other through a specific bus, the *Bus Interface (BI)*. The LEBs incorporate a CAN Interface card (CI), which consists of a CAN driver (DRV), an opto-coupled interface (OI) and a CAN controller (CC), that allows the LEBs

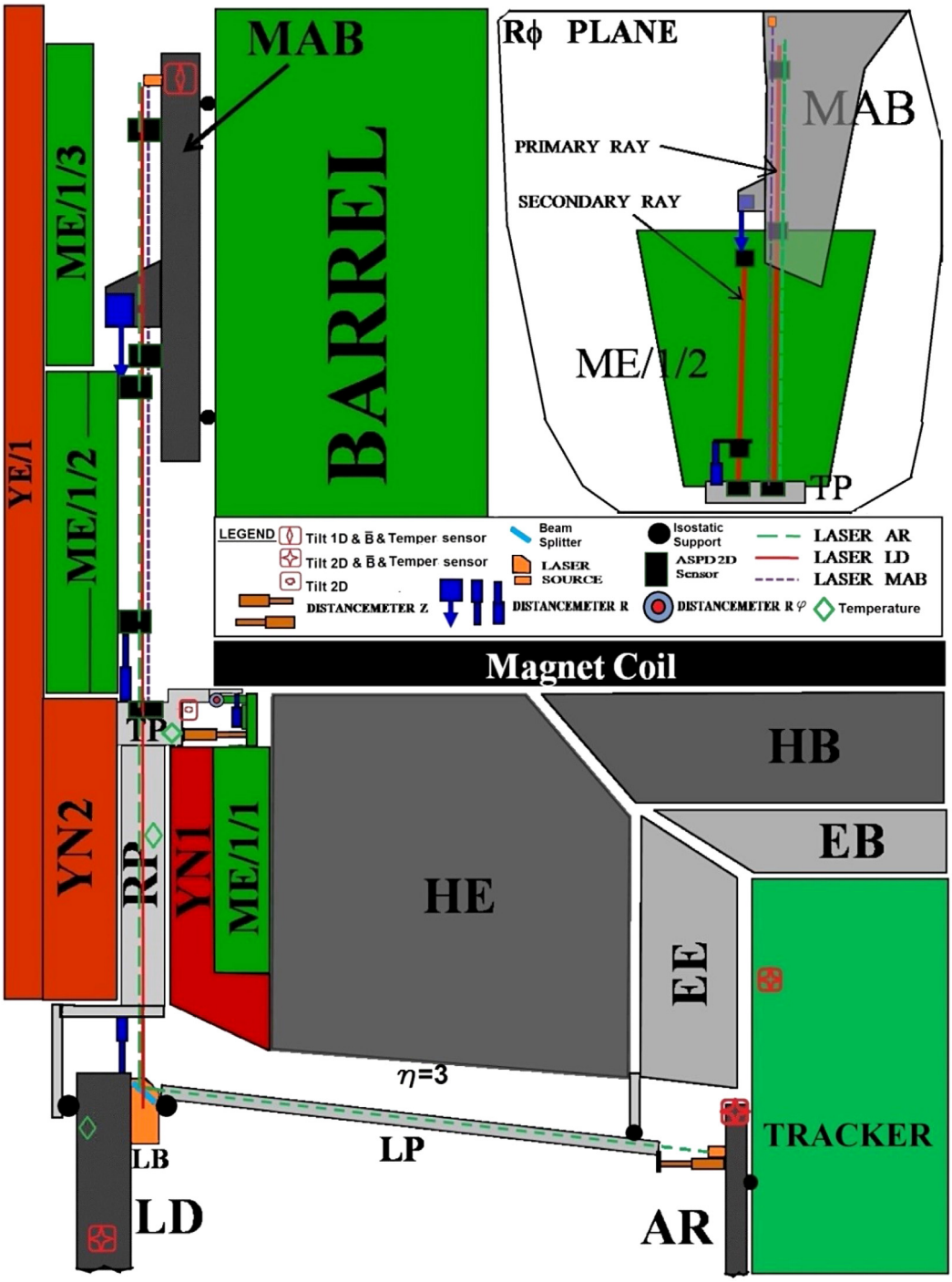

Fig. 9. Sketch of main Link Alignment elements (*R-Z* view, not to scale) in a quadrant of a *Φ* plane. The inset drawing shows the *Rϕ* projection of the Link System in the vicinity of the external MAB, showing the two Light Lines emerging from the Link Disk collimator.

to communicate with other LEBs and with a central PC via the CANbus communication protocol.

An *ASPD Control Interface (ACI)* generates and sends control signals to up to 4 remote ASPD sensors. The ASPD *Signal Conditioner (ASC)* converts output currents to voltage and adapts the voltage levels to the ADC input voltage range. The current to voltage conversion proceeds in two steps. First, a high precision resistor is used as feedback of an operational amplifier in order to convert current to voltage. In the second step a variable-gain amplifier adapts the signal to the ADC input range. Gains are adjustable and may be different for each sensor in a chain and even different for horizontal and vertical strips in a given sensor. In this way, at the beginning of a CMS data run gains, and laser output power are adjusted as needed.

To overcome eventual environmental radiation effects (including latchup), fault tolerant mechanisms are implemented by a *Redundant Controller System* with a *Fault Tolerant Interface (FTI),* which controls the LEB operation in a redundant mode. It includes two *Micro Controller Units* (*MCU*, Hitachi, H8S/2357) and the interface between them.

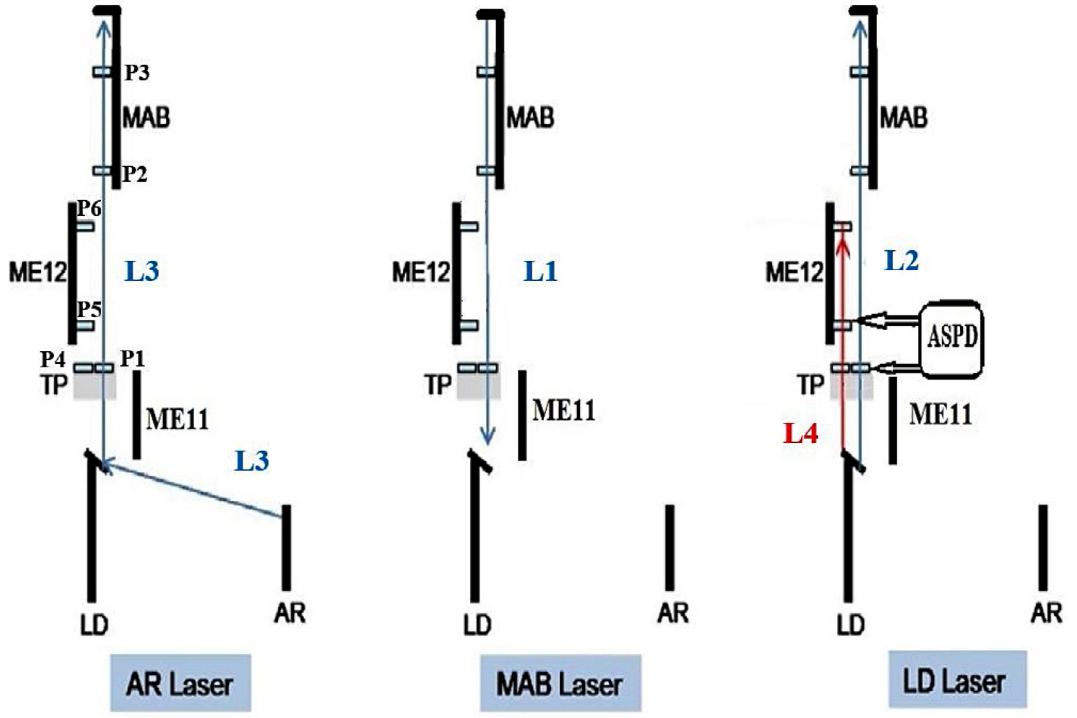

Fig. 10. Labelling of the four laser lines (L1 to L4) and the six ASPD (P1 to P6) sensors in a Φ link alignment quadrant. For each measurement, the three lasers are successively turned on.

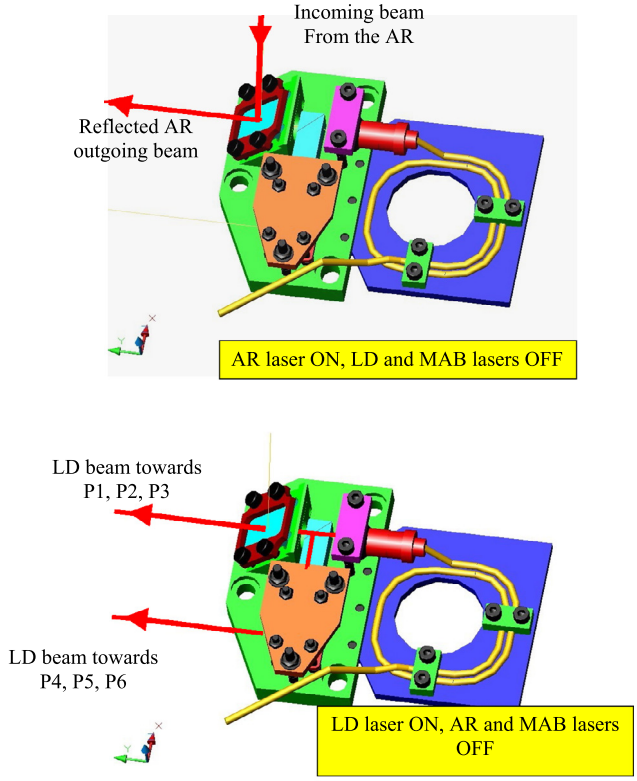

Fig. 11. Sketch of a Laser Box (LB) and its operation mode.

A *Fault Injection board interface (FI)* is used to program the MCUs via an RS-232 serial port. It controls fault injection procedures and communicates with an external application.

Table 1
Average characteristics of the ASPD sensors for the CMS Alignment System.

Sensitivity (mA/W)	16.3 ± 7.6
σ_x (μm)	5.2 ± 2.6
σ_y (μm)	5.1 ± 2.4
θ_x (μrad)	−1.1 ± 5.1
θ_y (μrad)	0.8 ± 3.8
Transmittance (%)	84.8 ± 2.9

Finally, a *Programming Interface (PI)* allows one to configure the MCUs programming. It supports two programming modes: via PC and cloning through the FI board.

The photograph in Fig. 8(b) shows an uncovered LEB after mounting all of its components.

6. Sensor performance and testing

A total of 122 ASPD units were constructed following the processes explained in Ref. [11]. An experimental procedure was developed in order to fully characterize the performance of each of the sensors prior to installation in the CMS detector. Results of this characterization are reported in Ref. [12]. From the total sample 72 sensors were installed in the detector, 36 per CMS Z side; 50 were left as spares.

In Table 1 the average performance of the 122 sensors show a photosensitivity of 16.3 ± 7.6 mA/W and a spatial point resolution of $\sigma_x = 5.2 \pm 2.6$ μm and $\sigma_y = 5.1 \pm 2.4$ μm. For a beam of light at perpendicular incidence to the given sensor face, the deflection angles where $\Theta_x = -1.1 \pm 5.1$ μrad and $\Theta_y = 0.8 \pm 3.8$ μrad, where Θ_x and Θ_y are the components along the x- and y-axis. The measured average transmittance T is 84.8 ± 2.9%. The most important construction parameters of the ASPD sensors, already discussed in Sections 3 and 4, are summarized in Table 2.

Those ASPD sensors and their associated electronics are designed to remain operative under the hostile environmental conditions of CMS such as high magnetic fields or high levels of irradiation. A clear confirmation of the robustness of the sensors is the observation that

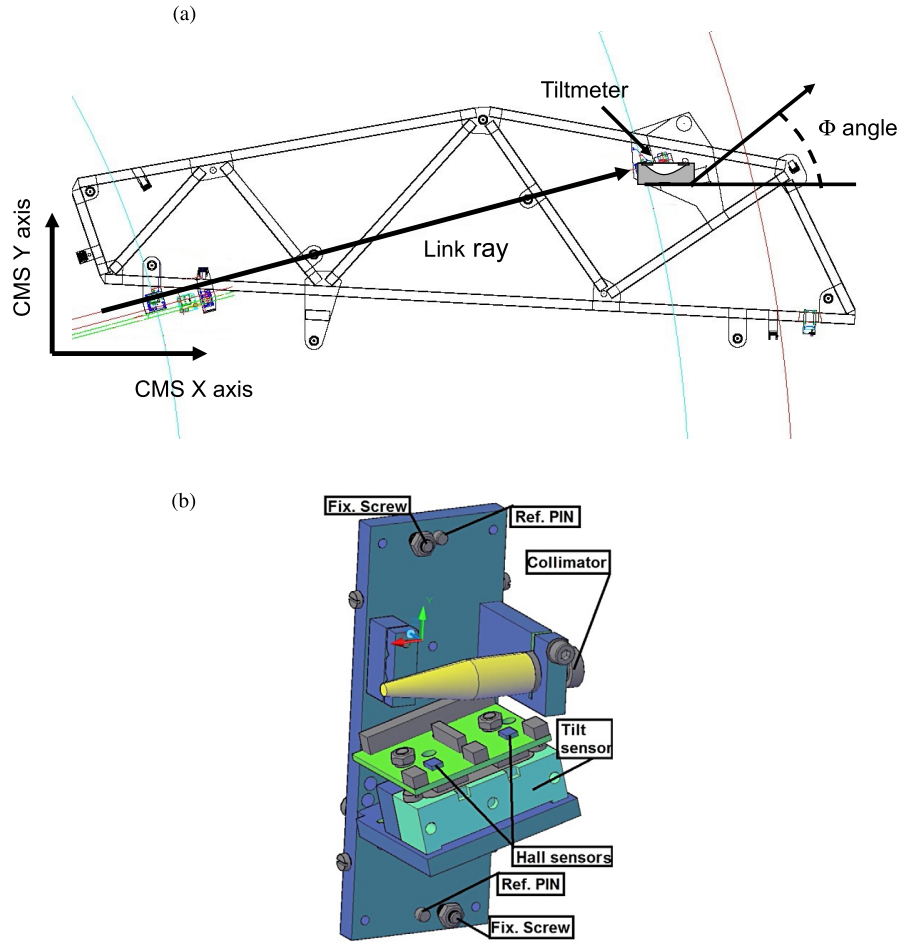

Fig. 12. Sketch of (a) an external MAB with the location of the tiltmeter inside the Laser Level and (b) the Laser Level (LL) mechanical structure containing one tiltmeter and one collimator.

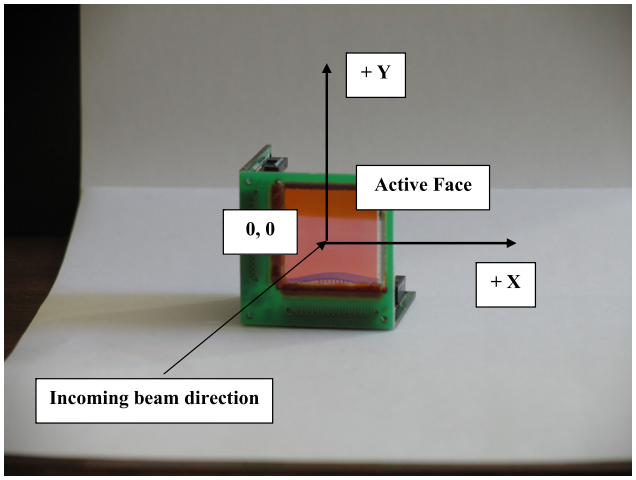

Fig. 13. Photograph of an ASPD sensor with its local axis system of coordinates and one example of possible incoming beam direction.

after more than seven years of operation in the CMS detector not a single ASPD sensor needed replacement.

The operation of the ASPD sensors is unaffected by the large magnetic field, since the short carrier-drift distance and the low Hall mobility of the amorphous silicon [11] has a small effect on the position resolution (i.e. less than 1 μm at 4 T).

Table 2
The ASPD construction parameters.

a-SiC:H thickness	195 nm
Strip thickness	110 nm
Glass thickness	1 mm
Active area	28×28 mm^2
Number of strips	64 horizontal + 64 vertical
Strip pitch	430 μm
Strip gap	22 μm

Irradiation tests, for the sensors and their FE electronics were performed with gamma rays at the NAYADE [13] facility at CIEMAT and with thermal neutrons at the MGC-20 Cyclotron of ATOMKI [14], in Debrecen. The results [15] proved that the a-Si material could withstand an irradiation up to 100 kGy photons (at a rate of 3 kGy/h) and up to $10^{15} \pm 37\%$ neutrons/cm^2 fluence without any degradation in the sensor performance.

The resistors and capacitors in the front-end electronics also remain operational after receiving these doses. Multiplexers (DG406, 16:1, from SILICONIX) are expected to be less radiation-hard than all other components, but, none of them have failed so far.

The most delicate component inside the LEB is expected to be the Microcontroller Unit so the behaviour of the Hitachi H8S/2357 MCU under photon and proton beams was investigated. Nine MCU devices were irradiated, in real operation conditions, with gamma-rays from a ^{137}Cs source at the IR14 facility of CIEMAT and with 60 MeV protons at the CYCLONE [14] installation of the Université Catholique

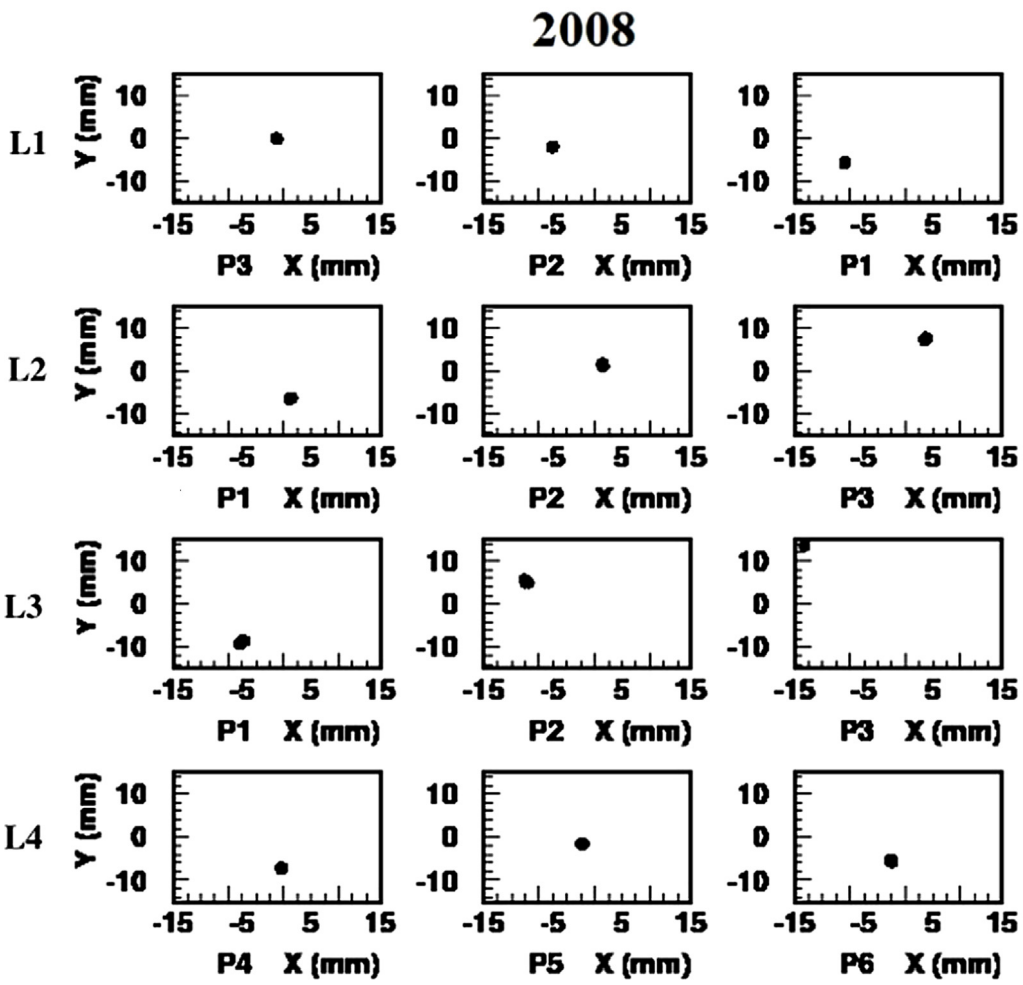

Fig. 14. Distribution of the (X, Y) reconstructed coordinates, at $\Phi = +75°$, of the 23 recorded ASPD events during the SP1 of the 2008 CMS operation. Rows correspond to the four laser lines, columns correspond to the sequentially crossed ASPD sensors.

de Louvaine (Belgium). The photon irradiation reached 210 Gy, and the total proton fluence was 1.5×10^{11} cm^{-2}.

The results [16] were very satisfactory: no malfunctions were detected due to the irradiation dose; during proton tests, only a few bit upsets in the SRAM memory occurred. No Single Event Latch-ups (SELs) were produced, and no Flash Memory or Single Event Effects (SEEs) were detected.

The most radiation-hard element of the configuration is the ASPD sensor. The associated LEB electronics, which is much less radiation tolerant, is located in the balconies of the CMS experimental area. The signal is carried from the ASPDs to the LEB ADC converter through more than 20 m long twisted pair cables.

7. Layout of photo sensors and diode lasers of the link alignment system

A sketch of one quadrant of a Φ Link alignment plane with its instrumentation is shown in Fig. 9. In each Φ quadrant six Amorphous Silicon Position Detector sensors (ASPDs) are connected by laser lines, as detailed in Fig. 10.

The four light paths of the network originate at the three collimators installed in each of the Φ quadrants, as sketched in Fig. 10. As an example, Light Path L2 starts at the collimator located in the Laser Box. The Laser Box (LB), attached to the Link Disk (LD), is a small optical bench (see sketches in Fig. 11) containing the LD collimator, a modified rhomboidal prism that splits the laser beam into two parallel beams about 5 cm apart, and a semi-transparent mirror that allows the LD laser light to pass through and reflects the laser beam (Light Path L3) coming from the AR.

The data taking procedure for each quadrant (see Figs. 10 and 11) is as follows. First, the AR laser turns on and the beam outgoing from the corresponding collimator (Light Path L3) arrives to the Laser Box mirror and is deflected to the sensors P1 (placed on the Transfer Plate), P2 and P3 (both located in the MAB). Distances are: d(AR-LB) = 3.682 m, d(LB − P1) = 2.151 m, d(P1 − P2) = 1.654 m, and d(P2 − P3) = 2.538 m. The total L3 Light Path length is then 10.025 m.

Then, the AR laser is switched off and the external MAB laser is turned on. The corresponding collimator, installed in the Laser Level (LL) attached to the MAB (see sketches in Fig. 12), sends a beam (Light Path L1) that crosses in sequence the sensors P3, P2 and P1. The distance between the collimator on the MAB and sensor P3 is 0.010 m.

Finally, the Laser Level (MAB Laser in Fig. 10) is switched off and the LD laser (whose collimator is installed in the LB) is turned on. The collimator in the Laser Box sends a beam that is split into two by the modified rhomboidal prism. One of the beams (Light Path L2) crosses the sensors P1, P2 and P3, while the second one (Light Path L4, parallel to the first one) crosses sensors P4 (at the TP), P5 and P6 (both attached to the ME/1/2 chamber). The distances are d(P4 − P5) = 0.067 m and d(P5 − P6) = 1.736 m.

The full sequence of lasers turning on and off, reading out of photocurrents in the sensors and reconstruction of the centres of the light spots on the ASPD surfaces constitutes a full data cycle set and takes slightly more than half an hour to complete.

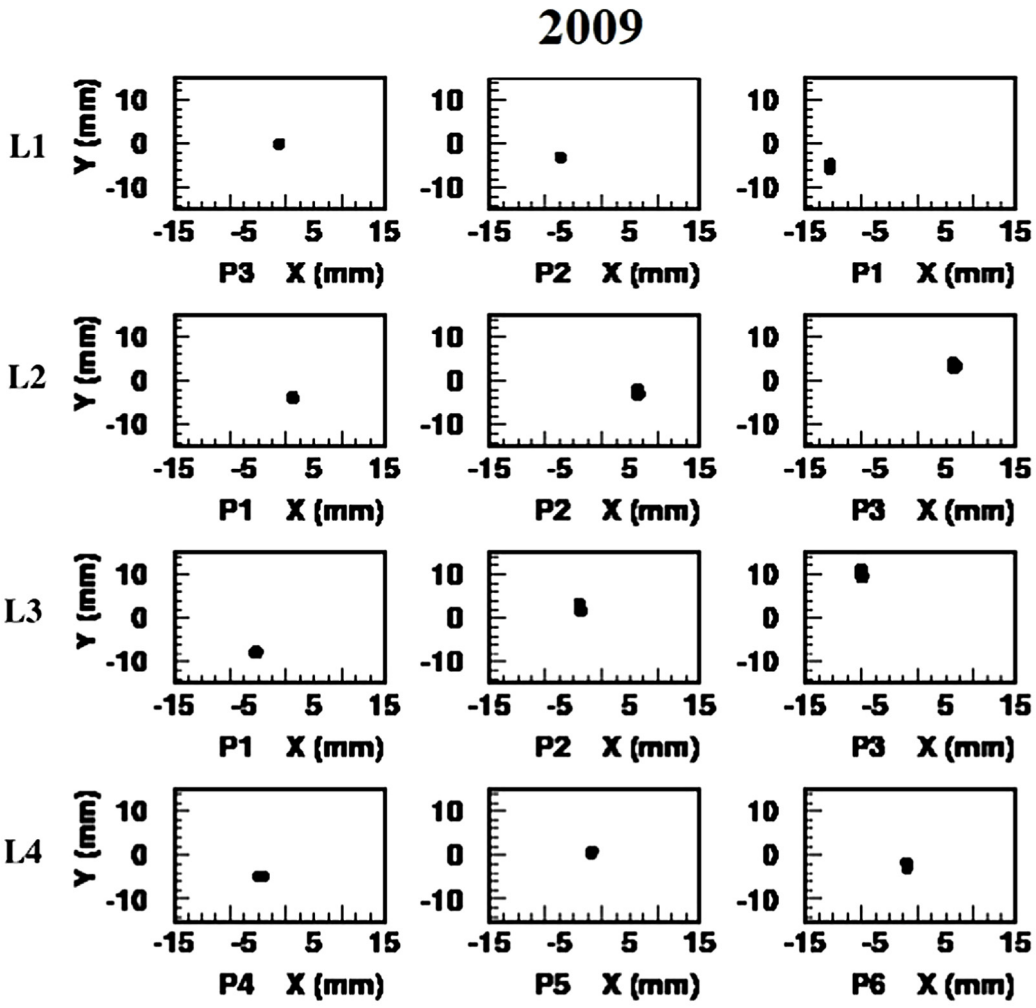

Fig. 15. Distribution of the (X, Y) reconstructed coordinates, at $\Phi = +75°$, of the 15 recorded ASPD events during the SP6 of the 2009 CMS operation. Rows correspond to the four laser lines, columns correspond to the sequentially crossed ASPD sensors.

7.1. Light spot resolutions

The laser beam in a given light path crosses a first sensor and then reaches a second with an incidence angle (in the X and the Y directions) that follows a Gaussian distribution with central value and width (rms) as measured in the characterization process of the first sensor. The reconstruction uncertainty in the second sensor, σ_2(rec), is therefore affected by an additional term, related to the uncertainty in the deflection angles, that can be written as: $\sigma_2^{\text{def}} = \sigma_1(\text{def}) \times d_{12}$ (where σ_1(def) is the width of the deflection angle distribution of sensor 1 and d_{12} the distance between sensors 1 and 2), to be added quadratically to the spatial reconstruction resolution of the second sensor.

The light ray is subsequently deflected in each of the downstream sensors in the given light path, always according to their measured values of deflection angles. In general, the resulting incidence angular distribution on the sensors surfaces is the convolution of the deflections happening successively in the upstream sensors, each of them having its own Gaussian-like distribution. The average deflection in sensor "j", due to the presence of several upstream sensors "i" ($i = 1, j-1$), can therefore be written as:

$$\Delta_j = \sum_{i=1,j-1} (\Theta_i \times d_{ij}) \tag{1}$$

where Θ_i is the deflection angle of sensor "i". The uncertainty induced in the reconstruction process in sensor "j" can be expressed as:

$$\sigma_j = \{\sigma_j^2(\text{rec}) + \sum_{i=1,j-1} [\sigma_i(\text{def}) \times d_{ij}]^2\}^{1/2} \tag{2}$$

The above expressions apply to both coordinates, X and Y.

The value of σ_j is precisely the resolution in the detection of displacements of the jth sensor in the line: the quantity that will determine whether a given sensor has moved or not from its initial position in the beam light. This quantity defines the spatial point reconstruction resolution of a given sensor inside its light path and will be used as the uncertainty in the light spot coordinates reconstruction. For the CMS network $j_{\max} = 3$.

The data recorded by the Optical System Network in the quadrant $\Phi = 75°$ at the $+Z$ side has been arbitrarily chosen to study the response of the ASPDs in operation for the years 2008 through 2013 and in 2015. A priori, there should be no difference in the behaviour of the different quadrants.

7.2. Characteristics of the sensors placed at the $\Phi = +75°$ quadrant

The six ASPDs placed in the $\Phi = 75°$ quadrant at the $+Z$ CMS side have the characteristics [12] shown in Tables 3 and 4.

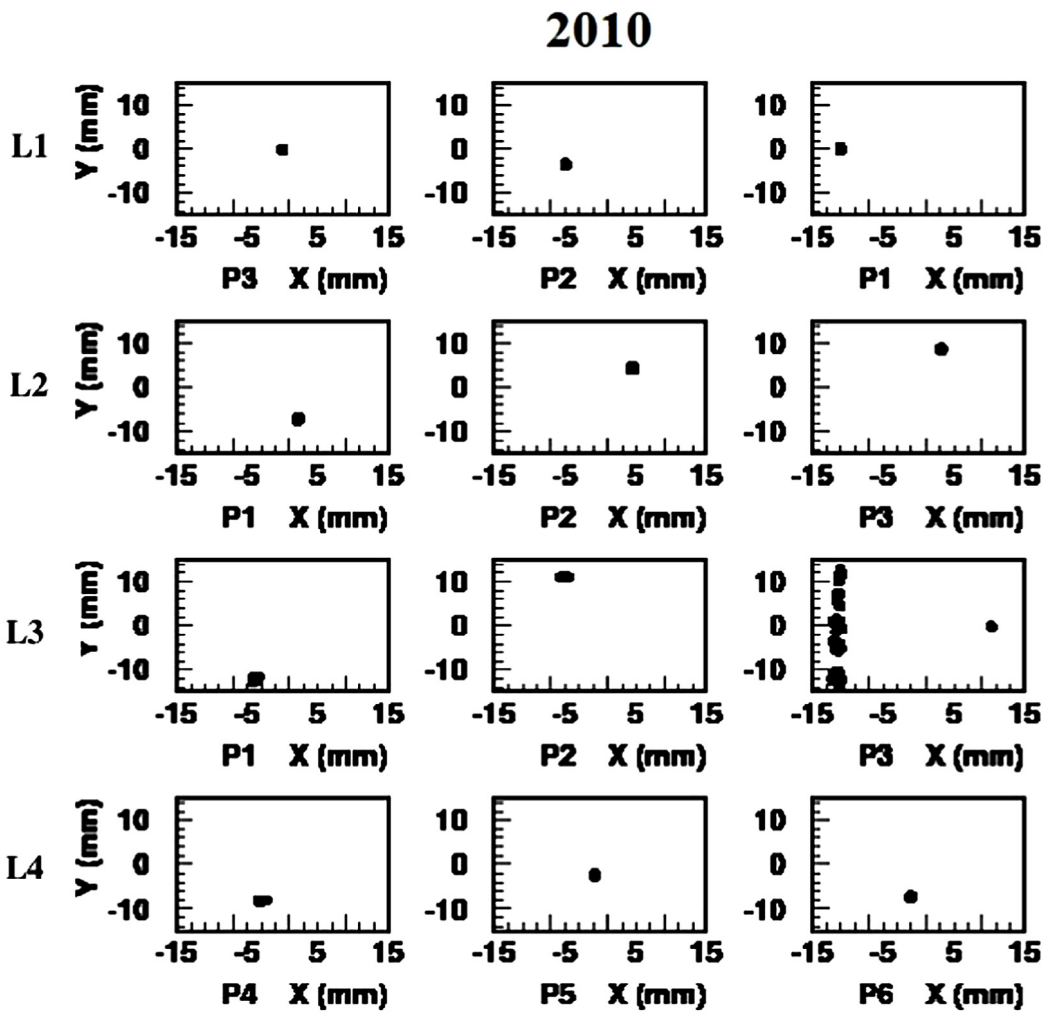

Fig. 16. Distribution of the (X, Y) reconstructed coordinates, at $\Phi = +75°$, of the 44 recorded ASPD events during the SP1 of the 2010 CMS operation. Rows correspond to the four laser lines, columns correspond to the sequentially crossed ASPD sensors.

Table 3
Characteristics of the photo-sensors labelled P1, P2 and P3 at $\Phi = +75°$.

Label	Characteristics	Active face	Glass face
P1	θ_x [μrad]	3.2 ± 1.9	3.7 ± 2.9
	θ_y [μrad]	2.2 ± 2.1	0.2 ± 4.9
	Transmittance (%)	86 ± 1	84 ± 2
	σ_x[μm]	7.4	8.7
	σ_y[μm]	5.4	11.3
P2	θ_x [μrad]	2.9 ± 4.3	1.4 ± 4.1
	θ_y [μrad]	4.0 ± 3.7	−2.5 ± 3.1
	Transmittance (%)	86 ± 1	85 ± 1
	σ_x[μm]	4.8	6.7
	σ_y[μm]	4.2	7.5
P3	θ_x [μrad]	−3.0 ± 5.7	−2.9 ± 3.2
	θ_y [μrad]	6.8 ± 5.2	−4.3 ± 7.1
	Transmittance (%)	85 ± 2	85 ± 1
	σ_x[μm]	5.9	7.0
	σ_y[μm]	4.4	4.4

Table 4
Characteristics of the photo-sensors labelled P4, P5 and P6 at $\Phi = +75°$.

Label	Characteristic	Active face	Glass face
P4	θ_x [μrad]	−3.7 ± 3.5	−5.0 ± 3.7
	θ_y [μrad]	2.8 ± 4.4	0.1 ± 2.7
	Transmittance (%)	85 ± 1	85 ± 1
	σ_x[μm]	6.4	6.3
	σ_y[μm]	2.9	4.4
P5	θ_x [μrad]	−5.2 ± 1.7	−6.4 ± 2.0
	θ_y [μrad]	0.1 ± 2.0	1.4 ± 2.0
	Transmittance (%)	76 ± 3	76 ± 3
	σ_x[μm]	6.9	6.2
	σ_y[μm]	3.2	3.0
P6	θ_x [μrad]	−5.1 ± 3.4	−5.8 ± 3.1
	θ_y [μrad]	4.6 ± 3.3	−3.6 ± 9.4
	Transmittance (%)	86 ± 1	85 ± 1
	σ_x[μm]	6.7	7.4
	σ_y[μm]	2.8	4.4

For ideal conditions Table 5 shows the calculated resolutions in the reconstruction of the various light spots for that quadrant, using the measured characteristics of the ASPD sensors, P1 to P6, crossed by the corresponding L1 to L4 laser lines [11]. All quantities appearing in Table 5 are given in micrometres.

The quoted uncertainties are calculated using Eq. (2), the measured sensor characteristics in Tables 3 and 4 and the appropriate sensor to sensor distances, *in ideal conditions*. This means that they represent the expected uncertainties in the absence of any major distortion of the laser light due to air density changes and assuming that the beam light arrives

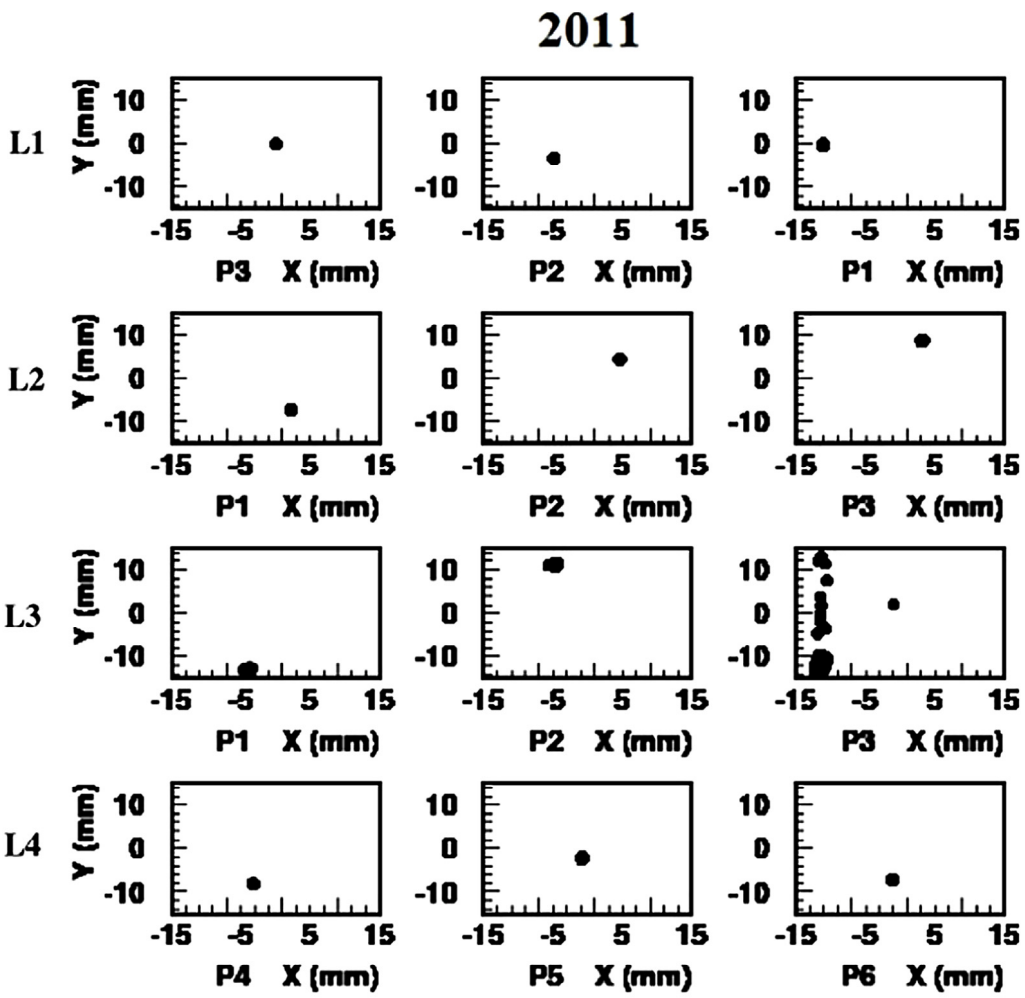

Fig. 17. Distribution of the (X, Y) reconstructed coordinates, at $\Phi = +75°$, of the 46 recorded ASPD events during the SP2 of the 2011 CMS operation Rows correspond to the four laser lines, columns correspond to the sequentially crossed ASPD sensors.

Table 5
Reconstruction resolutions (in μm) of the ASPD sensors in the X (σ_x) and Y(σ_y) coordinates, for the units placed in the $\Phi = 75°$ quadrant at the +Z CMS side, in ideal conditions.

Sensor resolutions	P1 σ_x/σ_y	P2 σ_x/σ_y	P3 σ_x/σ_y	P4 σ_x/σ_y	P5 σ_x/σ_y	P6 σ_x/σ_y
Light Path 1	10.0/7.4	10.5/19.5	7.0/4.4			
Light Path 2	8.7/11.3	6.8/9.1	12.4/10.4			
Light Path 3	8.7/11.3	6.8/9.1	12.4/10.4			
Light Path 4				6.3/4.4	6.9/3.2	7.3/4.5

Table 6
The column contents are: Observed year, Magnet Cycle containing the SP inspected, Stability Period in question, working magnetic field intensity, switch off conditions and number of recorded data events from the ASPDs, respectively. The first data considered during a SP is the one taken 24 h after the working magnetic field intensity is reached.

Year	Magnet Cycle nb. from Ref. [8]	SP nb. from Ref. [8]	B_{max} [T]	Switch off cond.	Total number of recorded ASPD events
2008	5	1	3.8	Controlled	23
2009	14	6	3.8	Controlled	15
2010	4	1	3.8	Fast Dump	44
2011	3	2	3.8	Fast Dump	46
2012	2	2	3.8	Fast Dump	187
2013	1	1	3.8	Fast Dump	64
2015	4	1	3.8	Fast Dump	30

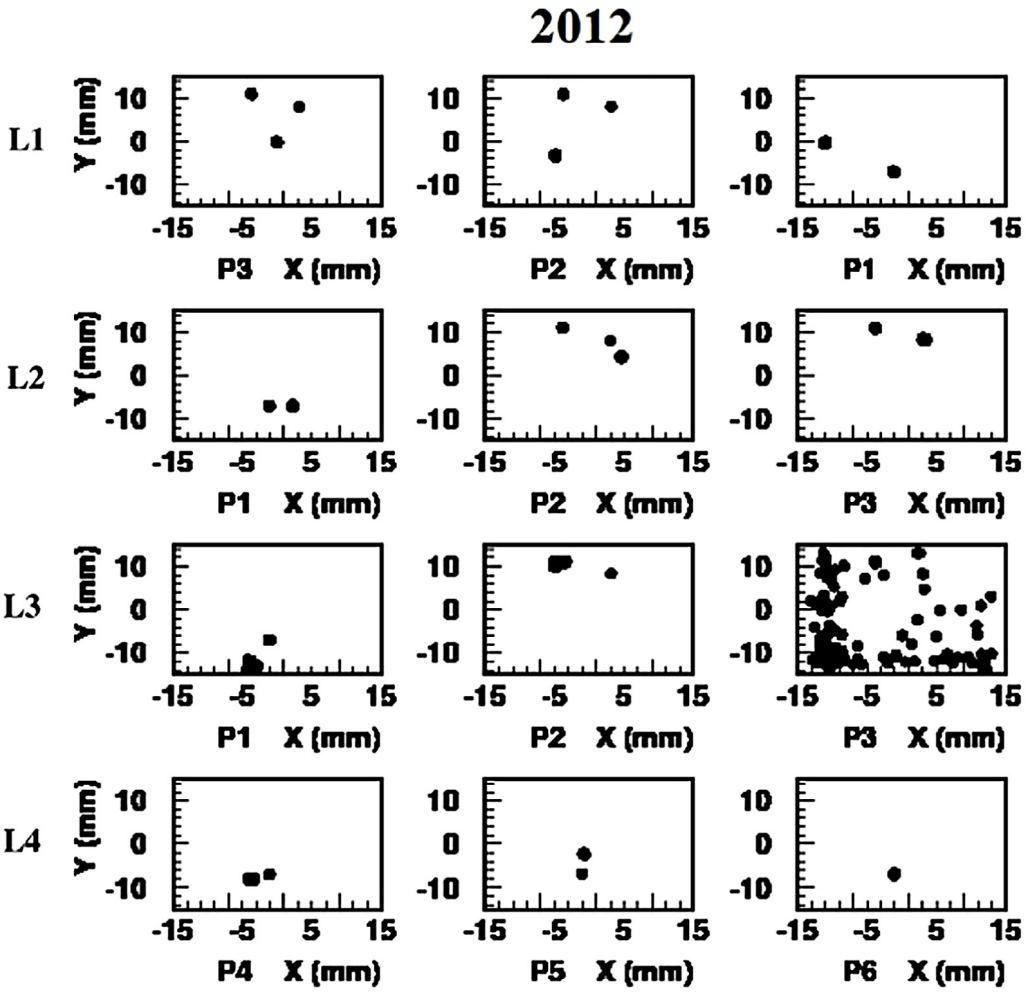

Fig. 18. Distribution of the (X, Y) reconstructed coordinates, at $\Phi = +75°$, of the 187 recorded ASPD events during the SP2 of the 2012 CMS operation. Rows correspond to the four laser lines, columns correspond to the sequentially crossed ASPD sensors.

in a direction approximately normal to the sensitive face and, of course, no mechanical motion of the rigid mechanical structures where they are attached. These requirements are rarely fulfilled by the laser light paths.

As mentioned, the distribution of photocurrents in the vertical (horizontal) strips are used to reconstruct the sensor local $x(y)$ coordinate of the light spot (see Figs. 6 and 7). The light spot reconstruction in the sensors is referred to their geometrical centre, whose coordinates are taken to be (0, 0). Since the strip pitch is 0.430 mm and the spot cannot be reconstructed beyond the centres of strips 0 and 63, the effective sensor limits are ±13.545 mm in both directions and the useable active area of an ASPD is then $\sim 27 \times 27$ mm^2.

The sensor coordinate system is sketched in Fig. 13: X- and Y-axis are the detector local coordinates. The beam in the figure is drawn incoming towards the active face of the sensor. In the Link System operation this is not always the case: there are sensors receiving the laser beam from the glass face side. Moreover, some of them receive laser light from both sides (although never simultaneously). The reception of light for one or the other sensor sides affects mainly the deflection angles, but not the light transmission, nor the light spot reconstruction. On the other hand, sensors on their supporting plates are attached to different CMS elements in different orientations, as can be inferred by looking at Figs. 9 and 10.

In fact, when the light spot reconstruction data are used in the COCOA reconstruction software [17] to determine the position of the photodetectors of the alignment network, the knowledge of the real space position of the physical ASPDs derived from the reconstruction of the light spots, is dominated by the uncertainty in their absolute spatial positions given by photogrammetry [6], about 300 μm for positions and 100 μrad for orientations.

Table 7
For the light line L1, RMS of the distribution of the distance between the first data, in the stability period under study (see Table 6), and each of the other data points, in each of the crossed sensors by light path, during a given year of CMS operation. RMS quantities greater than 300 μm are written in **bold**. When the RMS is greater than 900 μm (more than 3 σ away from stability) the amount is replaced by asterisks.

Light Line L1	Sensor P3	Sensor P2	Sensor P1
Year	RMS (μm)	RMS (μm)	RMS (μm)
2008	0.5	12.5	11.0
2009	0.9	10.9	**447.1**
2010	0.9	72.7	74.8
2011	1.6	44.6	49.9
2012	****	****	****
2013	1.9	10.8	17.8
2015	****	8.3	**588.9**

COCOA (CMS Object oriented Code for Optical Alignment), is an object oriented C++ software that handles the data provided by the CMS Alignment system and allows the reconstruction, at any moment, of the CMS geometry. For the Muon alignment system, COCOA might work with about 3000 parameters for the Link system, which are the possible positions and orientations of all the pieces that build up the system (distancemeters, collimators, prisms, ASPDs, tiltmeters, structures containing these systems, etc.). These parameters serve to

Table 8
For the light line L2, RMS of the distribution of the distance between the first data, in the stability period under study (see Table 6), and each of the other data points, in each of the crossed sensors by light path, during a given year of CMS operation. RMS quantities greater than 300 μm are written in **bold**. When the RMS is greater than 900 μm (more than 3 σ away from stability) the amount is replaced by asterisks.

Light Line L2	Sensor P1	Sensor P2	Sensor P3
Year	RMS (μm)	RMS (μm)	RMS (μm)
2008	44.5	81.3	164.3
2009	35.7	**423.2**	**446.1**
2010	18.7	54.7	68.9
2011	52.2	46.8	82.3
2012	**766.8**	****	****
2013	20.7	33.8	54.0
2015	11.8	17.6	27.7

Table 9
For the light line L3, RMS of the distribution of the distance between the first data, in the stability period under study (see Table 6), and each of the other data points, in each of the crossed sensors by light path, during a given year of CMS operation. RMS quantities greater than 300 μm are written in **bold**. When the RMS is greater than 900 μm (more than 3 σ away from stability) the amount is replaced by asterisks.

Light Line L3	Sensor P1	Sensor P2	Sensor P3
Year	RMS (μm)	RMS (μm)	RMS (μm)
2008	207.3	196.1	218.3
2009	112.5	**568.0**	**615.9**
2010	**348.1**	223.3	****
2011	260.3	260.5	****
2012	****	**819.1**	****
2013	99.3	160.8	****
2015	****	52.0	****

Table 10
For the light line L4, RMS of the distribution of the distance between the first data, in the stability period under study (see Table 6), and each of the other data points, in each of the crossed sensors by light path, during a given year of CMS operation. RMS quantities greater than 300 μm are written in **bold**. When the RMS is greater than 900 μm (more than 3 σ away from stability) the amount is replaced by asterisks.

Light Line L4	Sensor P4	Sensor P5	Sensor P6
Year	RMS (μm)	RMS (μm)	RMS (μm)
2008	33.2	41.0	71.5
2009	129.2	161.4	**373.9**
2010	104.9	17.6	26.6
2011	51.7	55.7	72.3
2012	**621.0**	****	74.6
2013	****	23.1	37.0
2015	****	****	22.5

Table 11
The repositioning, or difference between the X and Y reconstructed coordinates at $B = 0$ T before and after the Stability Period, in each of the three sensors in the Laser Path L1. Differences marked **** mean that at least one pair of point coordinates at $B = 0$ T was missing. No ASPD data at $B = 0$ T were recorded in the years 2013 and 2015.

ASPD	P3		P2		P1	
Year	ΔX_r [μm]	ΔY_r [μm]	ΔX_r [μm]	ΔY_r [μm]	ΔX_r [μm]	ΔY_r [μm]
2008	1	3	−40	79	−35	−98
2009	1	5	25	−27	13	−174
2010	−57	85	****	****	−36	−104
2011	1	−1	−2	−5	−39	−38
2012	1	−13	−57	121	**513**	****

actually constraint around 250 free parameters (declared as "unknown" or "calibrated" within certain error) inside the fitting code.

Table 12
The repositioning, or difference between the X and Y reconstructed coordinates at $B = 0$ T before and after the Stability Period, in each of the three sensors in the Laser Path L2. Differences marked **** mean that at least one pair of point coordinates at $B = 0$ T was missing. No ASPD data at $B = 0$ T were recorded in the years 2013 and 2015.

ASPD	P1		P2		P3	
Year	ΔX_r [μm]	ΔY_r [μm]	ΔX_r [μm]	ΔY_r [μm]	ΔX_r [μm]	ΔY_r [μm]
2008	−29	−23	−31	11	183	1
2009	−23	17	−70	−189	−146	−167
2010	−8	101	****	****	****	****
2011	51	127	105	1	−51	1
2012	−74	−150	−103	****	85	1

8. Light spots reconstruction and interpretation of motions

In what follows we will analyse some aspects of the data recorded by the ASPDs Link System Network, during the first seven years of CMS operation, for the indicated $\Phi = 75°$ quadrant of the $+Z$ CMS side.

In the positive CMS Z side (or $+Z$ side), photo sensors in the MABs are installed in such a way that a motion of the reconstructed light spot along the sensor $+X$ local axis corresponds to a displacement along the $+r\phi$ CMS coordinate of the physical sensor (the ASPD itself), and a motion of the reconstructed light spot along the sensor $+Y$ local axis corresponds to a displacement of the ASPD along the $-Z$ CMS coordinate.

For the ME1/2 sensors, a motion of the reconstructed light spot along the local $+X$ $(+Y)$ axis of the sensor corresponds to a displacement along the $-r\phi$ $(+Z)$ CMS coordinate of the physical sensor.

For the ME1/1 Transfer plate sensors, a motion of the reconstructed light spot along the local $+X$ $(+Y)$ axis of the sensor corresponds to a displacement along the $+r\phi$ $(+Z)$ CMS coordinate of the physical sensor.

In the negative CMS Z side (or $-Z$ side), for the MAB sensors, a motion of the reconstructed light spot along the local $+X$ $(+Y)$ axis of the sensor corresponds to a displacement along the $+Z$ $(+r\phi)$ CMS coordinate of the physical sensor.

For the ME1/2 sensors, a motion of the reconstructed light spot along the local $+X$ $(+Y)$ axis of the sensor corresponds to a displacement along the $-Z$ $(-r\phi)$ CMS coordinate of the physical sensor.

For the ME1/1 Transfer plate sensors, a motion of the reconstructed light spot along the local $+X$ $(+Y)$ axis of the sensor corresponds to a displacement in the $-$Z $(+r\phi)$ CMS coordinate of the physical sensor.

Given that in principle the laser beam path is fixed, when looking at the Laser Path L1 at the $+75°$ Φ quadrant (see Fig. 10), a variation in the reconstructed $+X$ local coordinate of the light spot on the sensor P2 (or P3) would correspond to a rotation in the $+\Phi$ CMS coordinate of the given sensor while a variation in the reconstructed $+Y$ local coordinate of the light spot on the sensor corresponds to a displacement in the $-$Z CMS coordinate of the sensor.

In the same way, a variation in the reconstructed $+X$ local coordinate of the light spot on the sensor P1 would correspond to a rotation in the $+\Phi$ CMS coordinate of the given sensor while a variation in the reconstructed $+Y$ local coordinate of the light spot on the sensor corresponds to a displacement in the $+Z$ CMS coordinate of the sensor.

Therefore, for two reconstructions of the light spot done at different times, 1 and 2, the interpretation in terms of the CMS variables, at the $+Z$ CMS side, for the sensors P2 and P3 are:

$$\text{arctg}((X_2{}^{\text{spot}} - X_1{}^{\text{spot}})/\text{RPI}) = \Delta\Phi_{\text{sensor}} \quad (\text{with } I = 2, 3)$$

where the R positions of the ASPDs are RP2 = 4.423 m and RP3 = 6.961 m and

$$-(Y_2{}^{\text{spot}} - Y_1{}^{\text{spot}}) = \Delta Z_{\text{sensor}}$$

While for sensor P1:

$$\text{arctg}((X_2{}^{\text{spot}} - X_1{}^{\text{spot}})/\text{RP1}) = \Delta\Phi_{\text{sensor}}, \quad \text{with RP1} = 2.151 \text{ m}$$

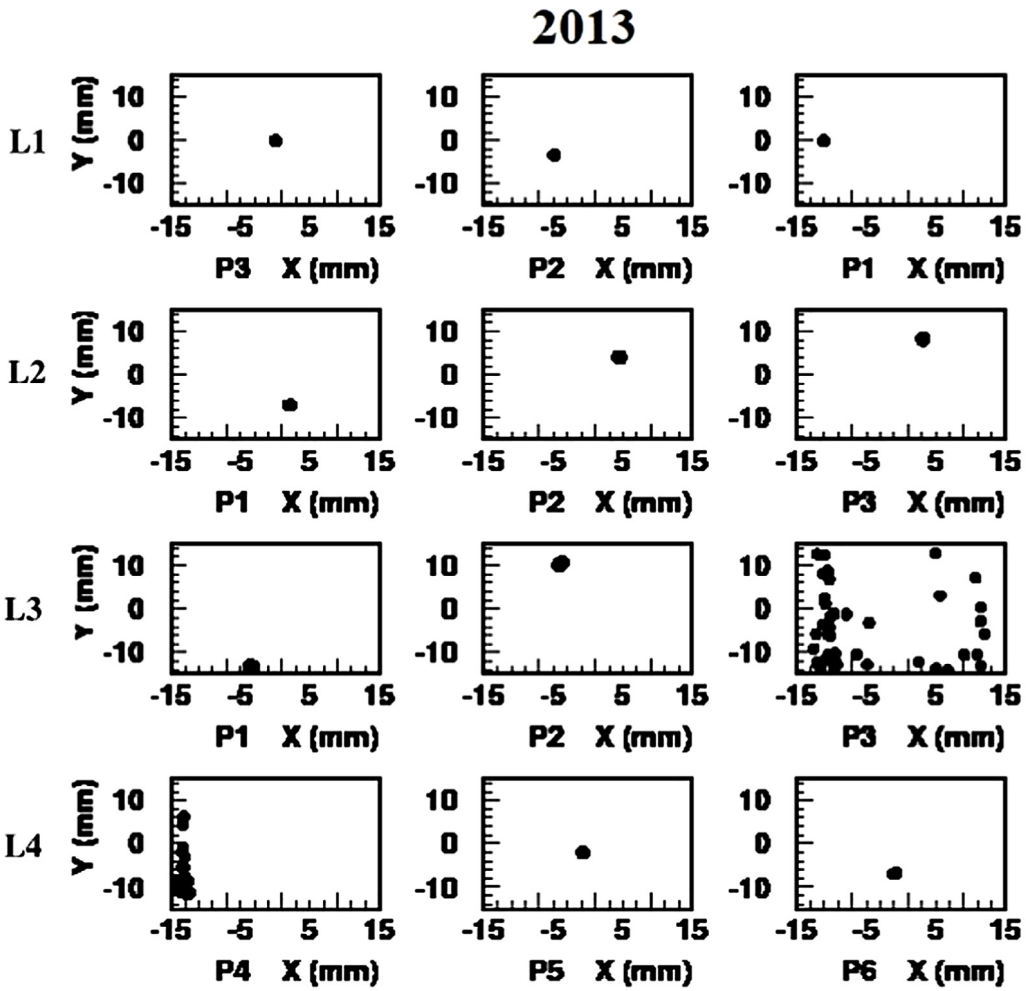

Fig. 19. Distribution of the (X, Y) reconstructed coordinates, at $\Phi = +75°$, of the 64 recorded ASPD events during the SP1 of the 2013 CMS operation Rows correspond to the four laser lines, columns correspond to the sequentially crossed ASPD sensors.

and

$$Y_2^{\text{spot}} - Y_1^{\text{spot}} = \Delta Z_{\text{sensor}}$$

The interpretation of the results is not unique, since the measured relative displacements and/or rotations of sensors P1, P2 and P3 may be, as pointed out above, a consequence of the convolution of displacements and/or rotations of the following elements: MAB, TP, LD and AR. The complete interpretation can only be made by a full geometrical reconstruction of the whole set of Link data in a given event by the COCOA software.

Not all laser spots are correctly reconstructed. Sometimes, one or more lasers might miss their target, resulting in wide spots consistent with pure background. Other times, the sensors themselves can have several strips damaged by dirt or occasional strip readout failure. Clearly, badly reconstructed laser positions can severely bias the final geometry reconstruction, and therefore, for the laser spots the errors in the X and the Y positions are required to be smaller than 500 μm. This guarantees, in principle, a good light spot reconstruction. Only well-reconstructed spots are fed to COCOA.

Given that the laser beams travel long distances, go through polarizers, collimators and optical fibre junctions, some reconstructed spots might actually become quite wide, and a visual inspection of all reconstructed light spots is necessary to make sure we do not reject spots which might not pass the criteria due to an unusually large width but which otherwise look reasonable.

In the following subsections, the reconstructed light spot coordinates on the various ASPDs originated by the four laser lines at the indicated Φ quadrant is studied over the seven years of operation. For simplicity, the discussion, when dealing with motions, will be restricted to the displacements along ΔY_{sensor}, since the relative movements along this local coordinate always correspond to the same global CMS direction and are easier to interpret without the need of a full reconstruction.

9. The behaviour of the ASPD data during CMS running

In Ref. [8], the general CMS mechanical motions during the Magnet Cycles and the structural equilibrium during the Stability Periods were investigated. A *Magnet Cycle* is defined as the operating time between the switching on and off of the current in the coils. During the ramping up of the current, from 0 to about 19 kA, the induced magnetic field in the solenoid goes from 0 to about 3.8 T. The enormous axial magnetic force pushing both CMS endcaps towards the geometrical centre of the detector induces important mechanical deformations/motions.

The structural equilibrium is achieved 24 h after the working magnetic field (3.8 T) is reached [7]. Structural equilibrium is defined as a period during which displacements in any direction (axial or radial) remain within the distance sensors resolution of ∼40 μm and any rotation will be smaller than the tilt sensors resolution of ∼40 μrad. Periods satisfying these constraints are called *Stability Periods* (SPs).

From the analysed data in Ref. [8] the present document will use the ASPDs records corresponding to the SPs presented in Table 6 and, when available, the data taken at $B = 0$ T immediately before and after the observed SP will also be used.

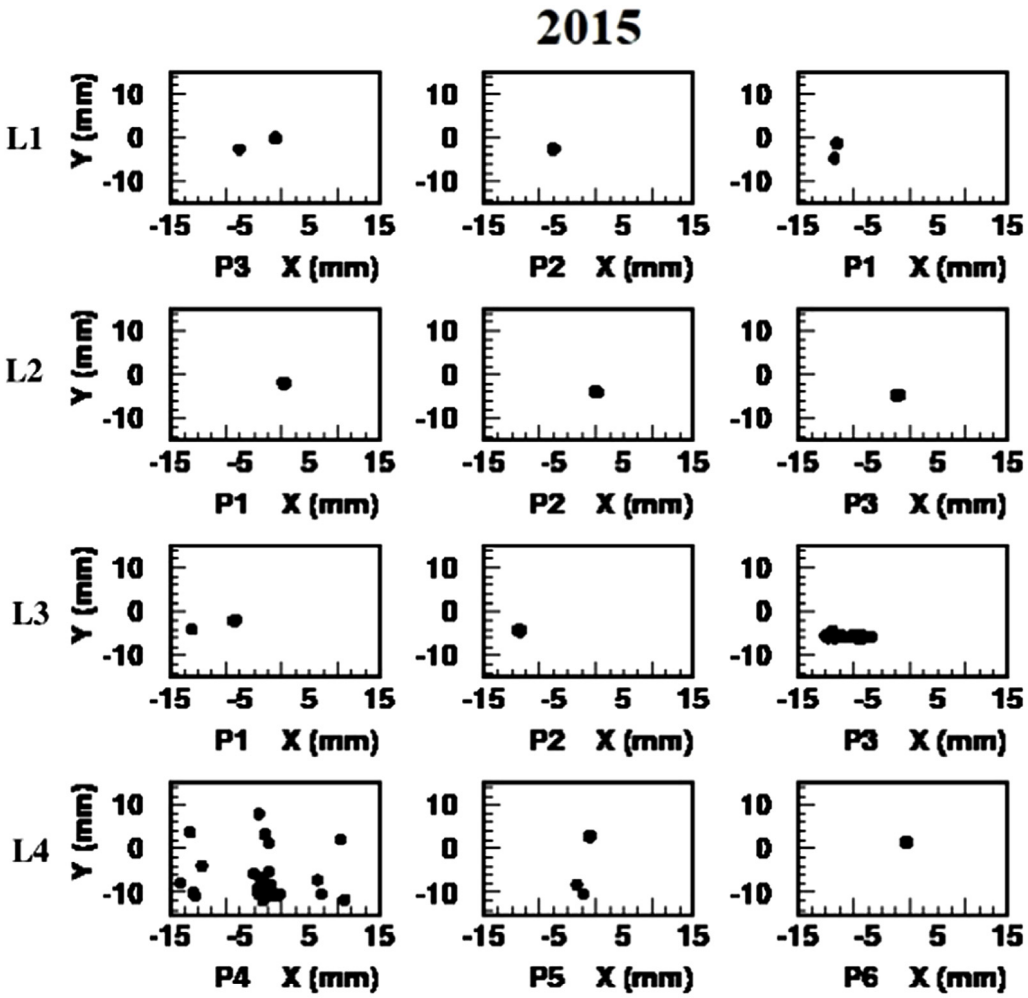

Fig. 20. Distribution of the (X, Y) reconstructed coordinates, at $\Phi = +75°$, of the 30 recorded ASPD events during the SP1 of the 2015 CMS operation. Rows correspond to the four laser lines, columns correspond to the sequentially crossed ASPD sensors.

The columns in Table 6 are the year, the Magnet Cycle containing the SP inspected, the Stability Period when the data are taken, the working magnetic field intensity, the switch off conditions and the number of ASPDs recorded events in that SP, respectively. The first data analysed during a SP is the one taken 24 h after the working magnetic field intensity is reached. In one day a maximum of two full ASPD data events (72 photo sensors, 144 light spots reconstructed coordinates) are recorded. There are days where no data are recorded.

In what follows the data taken from the photo sensors network, both during stability periods or magnet cycles, is studied and discussed.

9.1. Stability periods

To inspect possible motions of the photosensors during Stability Periods the following two items are investigated: the spatial distribution of the reconstructed light spots on the sensors surface (no distinction between active or glass sides) and the results from a clustering analysis of the impact points.

9.1.1. ASPD data during the stability periods

Figs. 14–20 show the reconstructed light spots during the Stability Periods (see Table 6) in the years 2008 to 2015, respectively.

Each row in the figures corresponds to one of the four Light paths, L1 to L4, shown in Fig. 10. L1 crosses in sequence sensors P3, P2 and P1 (plots in columns 1 to 3 on the first row, respectively). Light paths L2 and L3 do the same through P1, P2 and P3 (plots in columns 1 to 3 on the second and the third rows, respectively). Light path L4 crosses ASPDs P4, P5 and P6 (plots in columns 1 to 3 on the last row, respectively). In each of the three drawings in a given row the beam spots are represented by their X and Y, local to the corresponding sensor, reconstructed coordinates.

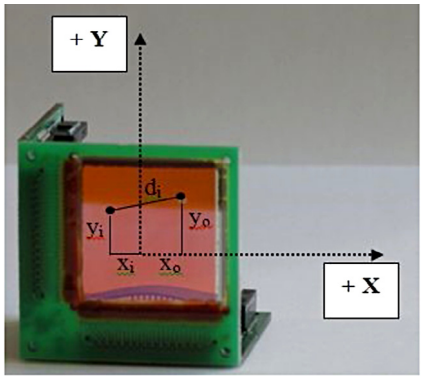

Fig. 21. Geometrical distance, d_i, between the reconstructed (x_i, y_i) coordinates of the light spot number i and the first (x_o, y_o) light spot on a given sensor P of a given laser line in the Stability Period under study. The origin of coordinates is the point (0, 0) of the sensor's active area. The reference (x_o, y_o) coordinates (inside the sensor surface) is irrelevant.

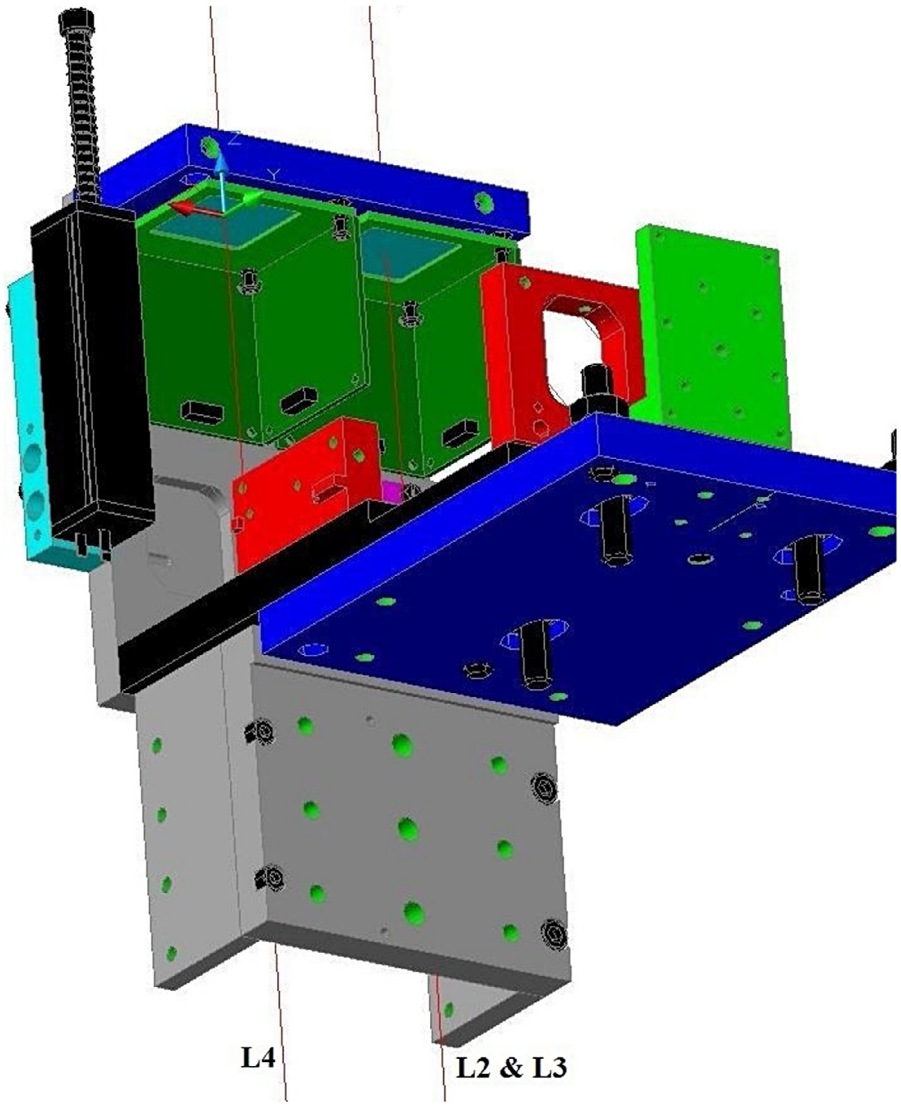

Fig. 22. Drawing of the Transfer Plate at the $\Phi = +75°$ quadrant. The left straight line represents the Light Path L4 crossing ASPD P4. The right straight line corresponds either to L2 or L3 Light Paths crossing ASPD P1. Lines are parallel and about 5 cm apart from each other.

To use the same scale for all twelve plots and for all years, we choose a large range which covers most of the sensor area, and, as a result, very often the dots are printed on top of each other. The number of entry pairs of (X, Y) spot coordinates are 23, 15, 44, 46, 187, 64 and 30 for the years 2008 to 2015, respectively, as shown in Table 6.

From the observation of these figures, the reader may suspect that certain degradation can be observed as time goes by. For example, the distribution of reconstructed light spots on sensor P3 in the line L3 from the year 2010 and onwards looks almost random. However, the response of the same sensor in the line L2 does not show any suspicious behaviour. The most probable explanation is that after the CMS closing before the 2010 physics run, the collimator sitting at the AR in the quadrant $\Phi = +75°$ became slightly mechanically unstable, allowing small oscillations, most probably due to air currents originated by temperature changes near the Tracker endcaps. It is important to notice that the Tracker was installed in CMS prior to the 2010 physics run.

Since L3 is the longest and most complex light path of the system, small collimator oscillations could easily cause the laser beam to miss the target sensor. If this happens, the readout would only register background illumination and, as a result, the Gaussian fit to reconstruct the light spot centre becomes very unstable, causing the reconstructed beam spot positions to look essentially random.

The consequences of the oscillations are more evident in sensor P3 because is the most far from the L3 collimator, the last to be crossed in this light path. It happens that sometimes the fake coordinate is only the X as in Fig. 17, the Y as in Fig. 20, or in both of them (Figs. 18 and 19). In all of these cases a visual inspection of the light spot reconstruction is needed, as already said, before feeding any pair of coordinates to COCOA.

The peculiar light spot reconstructions on sensor P4 at the light path L4 in the last two years (2013 and 2015), showing points somehow parallel to the Y coordinate, may be caused by dust affecting some horizontal strips, resulting in a non-unique reconstruction of the Gaussian-like distributions, or spurious light reflections misidentified as originated by a laser beam.

None of these suspicious light spot reconstructions are used in the CMS geometrical reconstruction software, but, since there are 12 Φ sectors, the full data results are, as already pointed out, sufficiently redundant.

9.1.2. *Clustering of light spots*

From the reconstructed coordinates of the light spots displayed in Figs. 14 to 20, the distances on the active surfaces of the corresponding ASPD sensors between the first reconstructed spot and all the others in a given Stability Period were calculated.

Table 13
The repositioning, or difference between the X and Y reconstructed coordinates at $B = 0$ T before and after the Stability Period, in each of the three sensors in the Laser Path L3. Differences marked **** mean that at least one pair of point coordinates at $B = 0$ T was missing. No ASPD data at $B = 0$ T were recorded in the years 2013 and 2015.

ASPD	P1		P2		P3	
Year	ΔX_r [μm]	ΔY_r [μm]	ΔX_r [μm]	ΔY_r [μm]	ΔX_r [μm]	ΔY_r [μm]
2008	−232	**927**	**−526**	1	****	**−1156**
2009	−88	160	−154	****	−386	****
2010	**474**	39	****	****	****	****
2011	**438**	****	**514**	****	****	****
2012	**973**	****	1281	****	****	****

Table 14
The repositioning, or difference between the X and Y reconstructed coordinates at $B = 0$ T before and after the Stability Period, in each of the three sensors in the Laser Path L4. Differences marked **** mean that at least one pair of point coordinates at $B = 0$ T was missing. No ASPD data at $B = 0$ T were recorded in the years 2013 and 2015.

ASPD	P4		P5		P6	
Year	ΔX_r [μm]	ΔY_r [μm]	ΔX_r [μm]	ΔY_r [μm]	ΔX_r [μm]	ΔY_r [μm]
2008	−36	3	50	−46	58	−257
2009	35	32	26	34	9	98
2010	11	116	−4	128	−2	1
2011	−35	168	−53	153	−121	1
2012	**−453**	−104	82	**−655**	248	****

The distance between the first reconstructed spot (x_o, y_o) and that of number i is given by

$$d_i = \sqrt{[(x_i - x_o)^2 + (y_i - y_o)^2]},$$

where the pair (x_i, y_i) denotes the reconstructed coordinates of a light spot, as shown in Fig. 21. The distribution of the distances d in each of the sensors, for each of the light paths during a given year, was investigated.

The quantities obtained from the distributions are the mean value of d, which is useless since it depends on the arbitrary reference (x_o, y_o) used, and the RMS of the distribution of the d_i values. The RMS is the quantity that shows how close the reconstructed light spots are from each other and therefore, quantifies the stability of the laser beams over the observed year. A large RMS value may even be due to the existence of various d distributions because of changes in the laser beam direction for different reasons (among them: sensor or collimator displacement, CMS deformations, etc.).

The results are displayed in Tables 7 to 10. The set of reconstructed light spot coordinates can be considered stable if the RMS of the corresponding distribution of distances is smaller than the general 300 μm uncertainty. In all, Tables 7–10 shows what was discussed from Figs. 14–20; in most cases the numbers show a good stability in the reconstructed coordinates of the light spots for a given sensor in a given Light path. Discrepancies have understandable explanations and are not due to sensor malfunctions.

9.2. Magnet cycles

From the laser light spot reconstructions of the X and Y coordinates during the Magnet Cycles cited in Table 6, the following quantities were calculated: (1) the repositioning, or difference between the X and Y reconstructed coordinates at $B = 0$ T before and after the Stability Period in each of the sensors; and (2) the amplitude of the motion, or difference between the X and Y reconstructed coordinates at $B = 0$ T and $B = 3.8$ T due to the motions induced in the mechanical structures supporting photodetectors and laser collimators when the magnetic field increases from zero to the working intensity.

9.2.1. Repositioning

The repositioning, or difference between the X and Y reconstructed coordinates (denoted by ΔX_r and ΔY_r, respectively) at $B = 0$ T, before and after a given Stability Period, in each of the sensors, are given in Tables 11–14. Each table corresponds to one of the four Light Paths and their associated sensors.

Distances are given in microns. Quantities smaller than the assumed 300 μm spatial position uncertainty, denote a good reproducibility of the place occupied before the ramping up and down of the magnetic field intensity. When larger than this value, the quantity is printed in bold. Differences marked **** mean that at least one pair of point coordinates at $B = 0$ T was missing, either because of a non-accepted reconstruction or because the laser beam missed the sensor.

In spite of the fact that some of the $B = 0$ T conditions from 2010 onwards were uncontrolled, the light spots after the magnet cycle are reconstructed at a distance smaller than 300 μm from the light spot previous to the ramping up of current in the coils in about 90% of the cases. On the other hand, the instability problem of the AR collimator from 2010 onwards becomes very visible in Table 13.

9.2.2. Largest displacements

The largest displacement corresponds to the difference in the X and Y reconstructed coordinates between $B = 0$ T and $B = 3.8$ T due to the motions induced by the magnetic forces. ΔX_d and ΔY_d, are displayed in Tables 15 to 17 for the sensors in the Light Paths L1, L2 and L4, respectively. Light Path L3 does not provide reliable measurements due to the already cited AR collimator instability.

Notice that in Tables 15 to 17 the differences are given in millimetres. Uncertainties, which are not quoted, are assumed to be 300 μm, taken as the general reconstruction uncertainty.

Since the light paths are quite different from each other in length, environmental conditions (in particular the air density), collimators pointing with orientations far from that of perpendicular incidence, etc., the detected motions (or absence thereof) are not identically reproduced by the three investigated lines.

In addition, the quality of the response of the ASPDs themselves may change from beam path to beam path, due, in particular, to the nonuniform response over the full photo-sensitive area, most of the time related to the location of the nonworking strips with respect to the laser beam impact point.

The Light Paths are sketched in Fig. 10. The *largest displacement* results displayed in Tables 15 to 17 are, mostly, a consequence of the deformation sketched in Fig. 2. The displacement ΔY_d observed in the location of P1 (Table 12) corresponds essentially to the displacements in Z of about 10 mm towards the Interaction Point of both the Laser Box at the Link Disk, where the collimator is placed, and of the Transfer Plate (TP, see Figs. 9 and 22), where P1 (right sensor in Fig. 22) and P4 (left sensor in Fig. 22) are installed [7]. The TP is on top of the Radial Profile (RP) and attached to the YN2 iron yoke as shown in Fig. 9.

Similarly, the ΔZ displacement of the LD, where the Laser Box is installed, due to the deformation in Fig. 2, finds a $\Delta Y_d \approx -10$ mm motion in the reconstruction of the laser light spot on the sensor P2 (Table 16). An FEA analysis performed in 1997 before the iron disks were constructed shows that in the vicinity of the laser lines the deflection is expected to be ≈ 11 mm [2]. On the other hand, the external MABs cannot shift very much towards each other (just a couple of millimetres) because the barrel iron disks are compressed by the Z-stops and only move a small amount.

Finally, the $\Delta Y_d \approx 3$ (7) mm motion of the reconstructed light spot over the P5 (P6) surface (Table 17) in the light path L4 (collimator inside the LB of the LD) is a result of the convolution of two movements: the LB moves towards the IP by an amount of the order of 10 mm, and the ME/1/2 chamber also moves in this direction by a smaller amount, and also tilts in such a way that P6 stays behind in Z with respect to P5 (also a consequence of the deformation sketched in Fig. 2). All motions are therefore understood and within the expectations.

Table 15
The largest displacement, or difference between the X and Y reconstructed coordinates at B = 3.8 T at the beginning of the Stability Period and the ones reconstructed at $B = 0$ T before the ramping up in magnetic field intensity, for each of the three sensors in the Laser Path L1. Differences marked **** mean that at least one pair of point coordinates at $B = 0$ T or B= 3.8 T was missing. No ASPD data at $B = 0$ T were recorded in the years 2013 and 2015.

ASPD	P3		P2		P1	
Year	ΔX_d [mm]	ΔY_d [mm]	ΔX_d [mm]	ΔY_d [mm]	ΔX_d [mm]	ΔY_d [mm]
2008	0.001	0.002	−0.017	0.121	−0.288	−11.862
2009	−0.002	0.001	0.008	−0.347	−0.038	−9.982
2010	−0.001	0.001	****	****	−0.654	−10.301
2011	0.001	0.001	−0.018	−0.449	−0.675	−10.439
2012	0.001	−0.003	−0.036	−0.437	−0.111	−7.074

Table 16
The largest displacement, or difference between the X and Y reconstructed coordinates at B = 3.8 T at the beginning of the Stability Period and the ones reconstructed at $B = 0$ T before the ramping up in magnetic field intensity, for each of the three sensors in the Laser Path L2. Differences marked **** mean that at least one pair of point coordinates at $B = 0$ T or B= 3.8 T was missing. No ASPD data at $B = 0$ T were recorded in the years 2013 and 2015.

ASPD	P1		P2		P3	
Year	ΔX_d [mm]	ΔY_d [mm]	ΔX_d [mm]	ΔY_d [mm]	ΔX_d [mm]	ΔY_d [mm]
2008	0.051	0.378	0.424	−11.293	0.554	****
2009	0.057	0.239	0.312	−9.850	0.514	−8.341
2010	0.084	0.308	0.367	****	0.337	****
2011	0.054	0.120	0.295	****	****	****
2012	−0.018	−0.067	0.131	−7.023	0.050	****

Table 17
The largest displacement, or difference between the X and Y reconstructed coordinates at B = 3.8 T at the beginning of the Stability Period and the ones reconstructed at $B = 0$ T before the ramping up in magnetic field intensity, for each of the three sensors in the Laser Path L4. Differences marked **** mean that at least one pair of point coordinates at $B = 0$ T or B= 3.8 T was missing. No ASPD data at $B = 0$ T were recorded in the years 2013 and 2015.

ASPD	P4		P5		P6	
Year	ΔX_d [mm]	ΔY_d [mm]	ΔX_d [mm]	ΔY_d [mm]	ΔX_d [mm]	ΔY_d [mm]
2008	0.101	0.455	0.135	3.151	−0.177	7.791
2009	0.006	0.262	0.191	2.560	0.066	7.712
2010	−0.106	0.369	0.100	3.184	−0.169	****
2011	−0.107	0.199	0.100	3.016	−0.127	****
2012	−0.447	−0.009	0.145	2.267	0.091	5.844

Table 18
Fitted parameters for the quadratic functions in Figs. 23–25, for the years 2008, 2009 and 2011, respectively. In the fits, the used error for ΔZ was 40 μm (the Sakae potentiometer resolution). For ΔY_d they were taken from Table 5.

	a [mm/T^2]	b [mm/T]	c [mm]	χ^2/NDF
ΔZ(LD-AR) 2008	−0.469 ± 0.006	−2.218 ± 0.026	−0.018 ± 0.023	78/17
2009	−0.418 ± 0.008	−2.285 ± 0.029	−0.080 ± 0.016	172/14
2011	−0.350 ± 0.009	−2.369 ± 0.034	0.004 ± 0.020	1/6
ΔY_d(P2–L2) 2008	−0.596 ± 0.002	−0.788 ± 0.007	0.012 ± 0.004	614/9
2009	−0.560 ± 0.001	−0.810 ± 0.005	−0.028 ± 0.003	2025/14
2011	−0.537 ± 0.002	−0.790 ± 0.006	−0.001 ± 0.004	24/6
ΔY_d(P5–L4) 2008	0.330 ± 0.001	−0.351 ± 0.002	−0.005 ± 0.002	381/11
2009	0.269 ± 0.001	−0.205 ± 0.002	0.006 ± 0.001	2100/14
2011	0.224 ± 0.016	−0.051 ± 0.006	0.016 ± 0.004	10/6

10. Correlation of motions

In Section 9 we interpreted the ≈ −10 mm ΔY_d largest displacement of the sensor P1 (Laser Path L1, Table 15) in terms of the expected deformation of the endcaps due to the magnetic field forces which cause displacements of both the collimator installed in the Laser Box (LB) located at the Link Disk (LD) and the Transfer Plate (TP) where the sensor P1 is installed (Fig. 22). In the present section some of the ΔY_d displacements are studied as a function of the magnetic field strength.

During the ramping up of the solenoid, data from some ASPDs and from short distance measurement sensors which monitor the axial AR to LD distance were simultaneously recorded, in the years 2008, 2009 and 2011. These data sets are shown in Figs. 23, 24 and 25, respectively. Data from other years were not taken due to the slow data-taking cycle for the ASPDs.

The dots in the figures represent the measured ΔZ(LD−AR) axial motion of the Link Disk towards the Alignment Ring as a function of the magnetic field intensity B (T). This distance is measured using a

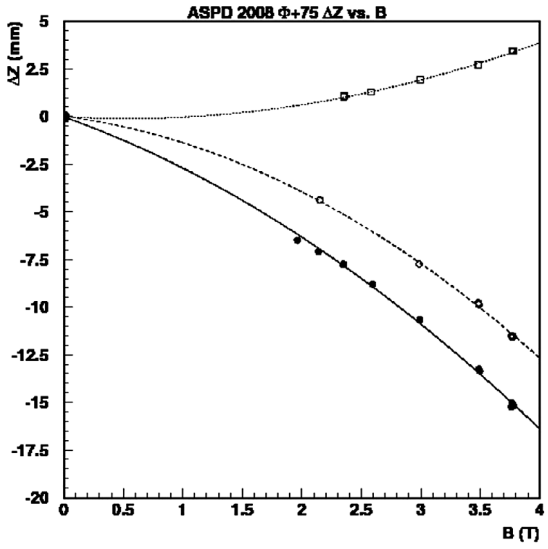

Fig. 23. During ramp up in magnet intensity in 2008: motion ΔZ(LD-AR) (dots), ΔZ(LD&TP) with respect to the Interaction Point as seen from P2 in the laser path L2 (circles) and motion of ME/1/2 with respect to LD as seen from P5 in the laser path L4 (squares).

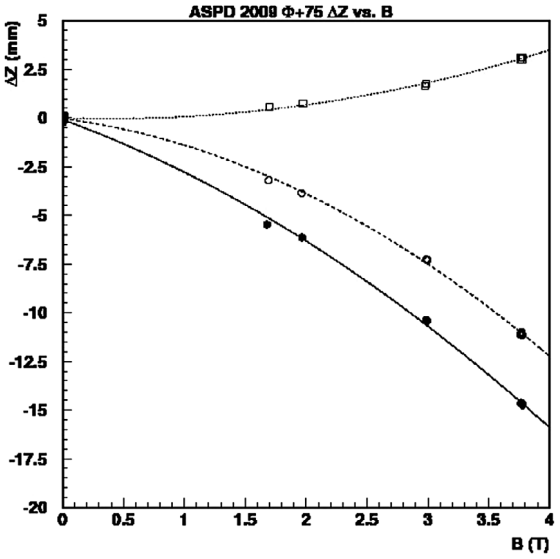

Fig. 24. During rump up in magnet intensity in 2009: motion ΔZ(LD-AR) (dots), ΔZ(LD&TP) with respect to the Interaction Point as seen from P2 in the laser path L2 (circles) and motion of ME/1/2 with respect to LD as seen from P5 in the laser path L4 (squares).

short distance Sakae potentiometer [18,19]. The open circles are the corresponding ΔY_d of the reconstructed Y coordinate of the L2 light spot over the P2 sensor surface, namely, the ΔZ motion of the TP towards the IP. At $B_{\max}$, the ΔZ motion of the TP towards the IP is smaller than the approach of the LD towards the AR measured by the potentiometer installed at the AR (see Fig. 9). This is due to the resistance of the Z-stops located between the endcap disks and the barrel region (see sketch in Fig. 2). The difference is of about 3.5 mm in the three examples below. The squares correspond to the motion of the laser beam light spot over the ASPD P5 when crossed by the Light Path L4, indicating the relative motion between the ME/1/2 muon chamber and the LD described at the end of the previous section. The difference in sign is the result of the

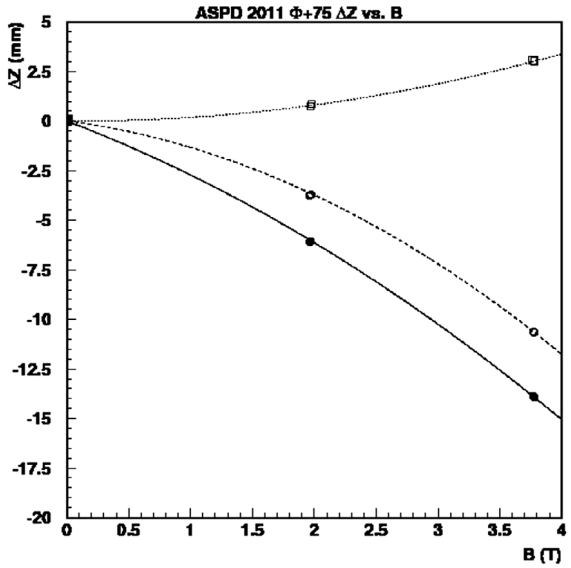

Fig. 25. During rump up in magnet intensity in 2011: motion ΔZ(LD-AR) (dots), ΔZ(LD&TP) with respect to the Interaction Point as seen from P2 in the laser path L2 (circles) and motion of ME/1/2 with respect to LD as seen from P5 in the laser path L4 (squares).

difference in the orientation of the local Y coordinate between the P2 and the P5 sensor. At $B_{\max}$ the measured motion is of about 3 mm.

The curves are all functions of the type $a \times B^2 + b \times B + c$ fitted to the data. The fitted constants are displayed in Table 18. The uncertainties used in the fit come from the data in Table 5, and the nominal resolution of 40 μm for the distance sensors (potentiometers).

The χ^2/NDF values indicate that the uncertainties used in the fit (i.e. those of ideal environmental conditions in Table 5), were underestimated. In fact, systematic errors such as the effects of temperature, motions and possible deformations of some parts of the system were not taken into account. However, the fitted parameters to the different data points are in fair agreement with each other in the various years.

The different values for the NDF in the three fits in the year 2008 are due to the fact that 8 light point reconstructions over the P2 sensor crossed by the Light Path L2 and 6 over the P5 sensor crossed by the Light Path L4 were of a poor quality and therefore discarded.

11. Summary

The network of laser lines and photosensors is the central feature of the CMS Link Alignment system that, in turn, is an important part of the general CMS Alignment system. The alignment provides a precise geometrical description of the detector, necessary to achieve the desired accuracy in the reconstruction of tracks from charged particles passing through an intense magnetic field.

The general layout of the semitransparent Amorphous Silicon Position Detectors (ASPDs), consisting of a matrix of perpendicular ZnO:Al (110 nm) strips sandwiching a layer of photosensitive Schottky photodiodes was introduced. The width of the conducting strips is 402 μm with 22 μm spacing between neighbouring strips. The total sensitive area is approximately 27×27 mm^2.

Prior to installation on the CMS detector, the measured performance, averaged over a sample of 122 units constructed, showed a sensor photosensitivity of 16.3 ± 7.6 mA/W, spatial point reconstruction resolutions of the light spot of $\sigma_x = 5.2 \pm 2.6$ μm and $\sigma_y = 5.1 \pm 2.4$ μm, deflection angles of $\Theta_x = -1.1 \pm 2.8$ μrad and $\Theta_y = -1.1 \pm 2.8$ μrad, and a transmission of $T = 84.8 \pm 2.9\%$.

The four light path lines and the six ASPD sensors per CMS Φ quadrant were described and details were given about the data taking

procedure. The protocol to perform a full recording cycle and to reconstruct the beam spots of the 72 ASPDs installed in CMS (36 per detector side) takes slightly more than half an hour.

An interpretation of the motions of the beam spots on the sensor surfaces was given, presenting examples of the motions detected during some Magnet Cycles and Stability Periods after the analysis of the ASPD data recorded over the years 2008–2013 and part of 2015, verifying the good performance of the sensors, which needed no replacements or repairs after more than seven years of operation.

In addition, the correlation between the CMS mechanical motions detected by the short distance measuring devices and those detected by the reconstruction of the light spots on the ASPD sensors during the ramping of the magnetic field were presented, demonstrating a good agreement and, therefore, that the ASPDs data are well understood.

The information provided by the network of photodetectors and diode lasers is an integral part of the Link alignment system and it is used in the COCOA simulation/reconstruction software to obtain the CMS detector geometry every time the CMS structures are closed and the detector is ready for operation. The present study extend the analysis of this network using all data collected by the system, thus providing a more deep understanding on the performance of this important component of the alignment system.

It can be concluded that our measurements confirm that the CMS Link alignment system performed as designed, and we anticipate the future monitoring of the muon system will continue to meet all specifications.

Acknowledgements

The authors thank the technical and administrative staff at CERN and all other CMS Institutes.

References

[1] The CMS Collaboration, The CMS experiment at the CERN LHC, J. Instrum. 3 (2008) S08004.
[2] The CMS Collaboration, The Magnet Project Technical Design Report, CERN/LHCC 97-10.
[3] The CMS Collaboration, The Muon Project Technical Design Report, CERN/LHCC 97-32.
[4] The CMS Collaboration, The Tracker Project Technical Design Report, CERN/LHCC 98-06.
[5] V. Karimaki, G. Wrochna, CMS TN/94-199; F. Matorras and A. Meneguzzo, CMS TN/95-069 and I. Belotelov, et al., CMS NOTE 2006/017.
[6] L.A. García Moral, et al., Nucl. Instrum. Methods A 606 (2009) 344.
[7] P. Arce, et al., Nucl. Instrum. Methods A 675 (2012) 84.
[8] P. Arce, et al., Nucl. Instrum. Methods A 813 (2016) 36.
[9] M. Sobrón, CMS Detector Geometry Reconstructed with the Link Alignment System (Ph.D. thesis), Instituto de Física de Cantabria, UC-CSIC, Santander, Spain, 2009.
[10] E. Calvo, Characterization of Mechanical Properties of Adhesive Joints Subjected to Radiactive Environments in Particle Detector Alignment Systems (Ph.D. thesis), ETS de Ingenieros Industriales y de Telecomunicación. Universidad de Cantabria, Santander, Spain, 2015.
[11] C. Khöler, et al., Nucl. Instrum. Methods A 608 (2009) 55.
[12] A. Calderón, et al., Amorphous Silicon Position Detectors for the Link Alignment System of the CMS Detector: Users Handbook, Informe Técnico Ciemat, Madrid : CIEMAT, 2007.
[13] http://www.ciemat.es/interno/eng/instalacion/0i070.html.
[14] A. Fenyvesi, et al., Z. Med. Phys. 1 (1991) 1.
[15] J. Cárabe, et al., Nucl. Instrum. Methods A 455 (2000) 361.
[16] G. Berger, G. Ryckewaert, R. Harboe-Sorensen, L. Adams, CYCLONE –A Multipurpose Heavy Ion, Proton and Neutron SEE Test Site, Abstracts for RADEC 97 W-25, Cannes France, 1997.
[17] P. Arce, A.L. Virto, CMS Object Oriented Code for Optical Alignment (COCOA), CMS IN 2002/060, 2002.
[18] Sakae Tsushin Kogyo Co. Ltd. - Trade Dept. 322 Ichinotsubo, Nakahara-ku, Kawasaki-city, Kanagawa-prefecture, 211-0016 Japan, http://www.sakae-tsushin.co.jp.
[19] A. Calderón, et al., Nucl. Instrum Methods A 565 (2006) 603.